1 **GLC_FCS10: a global 10-m land-cover dataset with a fine classification system from Sentinel-1**

2 **and Sentinel-2 time-series data in Google Earth Engine**

3 Xiao Zhang [1,2], Liangyun Liu [1,2,3*], Tingting Zhao [1,4], Wenhan Zhang [1,2,3], Linlin Guan[1,2], Ming Bai [1,5], and Xidong

4 Chen [6]

5 1 International Research Center of Big Data for Sustainable Development Goals, Beijing, 100094, China.

6 2 Key Laboratory of Digital earth Science, Aerospace information Research institute, Chinese Academy of Sciences,

7 Beijing, 100094, China.

8 3 School of electronic, electrical and communication engineering, University of Chinese Academy of Sciences,

9 Beijing, 100049, China.

10 4 School of Geography and Ocean Science, Nanjing University, Nanjing, Jiangsu 210023, China.

11 5 College of Geomatics, Xi'an University of Science and Technology, Xi'an 710054, China.

12 6 Future Urbanity & Sustainable environment (FUSE) Lab, the University of Hong Kong, Hong Kong, 999007,

13 China.

14 Corresponding author: Liangyun Liu (liuly@radi.ac.cn)

15 **Abstract**

16   The continuous development of remote sensing techniques provides ample opportunities for high-

17 resolution land-cover mapping. Although global 10-m land-cover products have made considerable progress

18 over past few years, their simple classification system makes it difficult to meet the needs of diverse applications.

19 In this work, we propose a hierarchical land-cover mapping framework to produce a novel global 10-m land-

20 cover dataset with a fine classification system (called GLC_FCS10) using Sentinel-1 and Sentinel-2 time-series

21 observations from 2023. First, the globally distributed training samples are hierarchically obtained from

22 multisource prior products after applying a series of refinements. Then, a combination of hierarchical land-cover

23 mapping, local adaptive modeling, and multisource features is used to produce land-cover maps for each 5 ×

24 5 geographical tile. Next, using 56121 globally distributed validation samples and a third-party validation

25 dataset (LCMAP_Val), the GLC_FCS10 is assessed. The GLC_FCS10 achieves an overall accuracy of 83.16%

26 and a kappa coefficient of 0.789 globally and an overall accuracy of 85.09% in the United States. Meanwhile,

27 comparisons with five released 10- or 30-m land-cover products also demonstrate that GLC_FCS10 has higher

28 accuracy and captures more diverse land-cover information than three of the released global 10-m land-cover

29 products. In summary, the novel GLC_FCS10 land-cover maps can provide important support for high-

30 resolution land-cover related research and applications. The GLC_FCS10 can be freely access via

31 https://doi.org/10.5281/zenodo.14729665 (Liu and Zhang, 2025).

32

1. Introduction

Land-cover information is a vital component of global climate change research and plays an important role in climate change mitigation, biodiversity protection, and global food security (Foley et al., 2005; Liu et al., 2021). With advancements in satellite techniques and computational and storage capabilities, global land-cover mapping has made substantial progresses. A series of global land-cover products, ranging from 1-km to 10-m resolutions, has been continuously released (Giri et al., 2013; Liu et al., 2021). Recently, Wang et al. (2023) reviewed the characteristics of global land-cover products and found that land-cover mapping has evolved from coarse to high spatial resolution. Currently, four global 10-m land-cover products are available, including FROM_GLC10 (Gong et al., 2019), ESRI LC (Karra et al., 2021), European Space Agency (ESA) WorldCover (Buchhorn et al., 2020), and Dynamic World (Brown et al., 2022). However, all of these products use a simple classification system, which limits their applicability for specific and fine applications (Zhang et al., 2021). Meanwhile, the work of Zhao et al. (2023) explained that FROM_GLC10, ESRI LC, and ESA WorldCover have relatively low consistency and accuracy. Thus, developing an accurate global 10-m land-cover dataset with a fine classification system is still necessary.

The diversity of land-cover types depends on the training samples, and there are two options to generate a globally distributed training pool—visual interpretation and automated derivation from prior products (Zhang and Roy, 2017; Zhang et al., 2021). Visual interpretation means that experts or volunteers interpreted the land-cover information through high-resolution imagery, Google Earth Streetview photos, or other auxiliary datasets. For example, the training samples in FROM_GLC10 were derived from expert interpretations and contained approximately 93,000 sites worldwide (Gong et al., 2013), and the ESA WorldCover used 20 trained experts to collect approximately 141,000 training locations from the Geo-Wiki engagement platform (Buchhorn et al., 2020). Obviously, training sites from the "visual interpretation" option can ensure high quality (Ban et al., 2015), however, the problems of cost and time are not to be ignored. The diversity of the land-cover classification system also relies on the experts' prior knowledges. The "automated derivation from prior products" option generates the training sites from prior land-cover datasets after taking some refinements or validations (Radoux et al., 2014; Zhang et al., 2021; Zhang et al., 2024c). For example, the training areas in the GLC_FCS30 were collected from a combination of time-series MCD43A4 surface reflectance data and CCI_LC land-cover products after using some spatiotemporal purification methods, and these automatically derived training samples supported high-accuracy land-cover mapping with overall accuracy of 82.5% (Zhang et al., 2021). The automated option enables more efficient collection of globally confident training samples; however, the classification errors of prior land-cover products were also easier to transfer into the derived training samples (Zhang and Roy, 2017). Therefore, it is critical to avoid transferring error into the training samples.

Another great challenge in global land-cover mapping lies in the choice of suitable methodologies. Currently, the vast majority of global land-cover mapping ignores the complexity and sparsity of various land-cover types and completes a mapping project with a single classification model (Friedl et al., 2010; Gong et al., 2013), which leads to considerable uncertainties in sparse (e.g., impervious surfaces) or complex (e.g., wetlands and shrubland) land-cover types (Karra et al., 2021; Zhang et al., 2021; Zhao et al., 2023). Several measures were taken to improve the performance of large-area land-cover mapping, such as: local adaptive modeling (Defourny et al., 2018; Li et al., 2023; Zhang and Roy, 2017; Zhang et al., 2021), hierarchical land-cover mapping (Chen et al., 2015; Sulla-Menashe et al., 2019), or integration of multisource datasets (Yu et al., 2014; Zhang et al., 2020).

Local adaptive modeling first split study area into many local areas and further trained corresponding classification models within each local region to improve the ability to capture regional characteristics. Zhang and Roy (2017) found that local adaptive modeling had higher accuracy than single global land-cover modeling, however, it also needs enough training samples to support regional modeling. Hierarchical land-cover mapping divides the

76 land surface into various land-cover layers, and some complicated land-cover layers may need to be treated
77 independently. Taking wetlands as an example, most global land-cover products perform poorly on wetlands because
78 of their varied spectral characteristics and complicated spatiotemporal features (Buchhorn et al., 2020; Gong et al.,
79 2019; Zhang et al., 2021). The GlobeLand30 achieved 74.87% accuracy with wetlands because this land-cover type
80 was treated independently (Chen et al., 2015). Hierarchical land-cover mapping gives more attention to complicated
81 land-cover types by importing more prior knowledge (Chen et al., 2015) or adding sufficient high-confidence training
82 samples (Zhang et al., 2023b). many previous works have demonstrated the integration of multisource datasets, such
83 as optical imagery (Landsat and Sentinel-2) and Sentinel-1 single-aperture radar (SAR) data to improve the
84 identification of impervious surfaces (Zhang et al., 2020), wetlands (Zhang et al., 2023b), forests (Tang et al., 2023),
85 or croplands (Blickensdörfer et al., 2022). Therefore, multisource data effectively enhances land-cover mapping.

86 The free access to Sentinel imagery and to the powerful cloud computation platform provide ample opportunity
87 for global land-cover mapping at 10 m. In this work, we developed an accurate and novel global 10-m land-cover
88 product (called GLC_FCS10) containing 30 fine land-cover types from Sentinel-1 and Sentinel-2 time-series imagery.
89 To achieve this goal, we propose: 1) a hierarchical land-cover mapping framework to decrease the uncertainties of
90 impervious surfaces and wetlands; 2) to combine the prior multisource land-cover datasets and the metric centroid to
91 automatically generate a globally distributed and high-confidence 10-m training pool; 3) to integrate time-series
92 Sentinel-2 optical and Sentinel-1 SAR data for producing the new GLC_FCS10 on the GEE platform; 4) to
93 comprehensively compare the developed GLC_FCS10 with several previous products.

94 **2. Datasets**

95 **2.1 Satellite imagery**

96 All available Sentinel-2 surface reflectance imagery for 2023 were atmospherically corrected using the Sen2Cor
97 tool, and the corrected images were then stored on the GEE platform. This imagery contains 12 spectral bands from
98 visible to shortwave infrared and a revisiting period of 5 days (Berger et al., 2012; Radeloff et al., 2024). In this work,
99 the four 10-m visible and near-infrared bands and six 20-m red edges and shortwave infrared bands were used, while
100 the two 60-m bands of aerosols and water vapor were excluded to minimize atmospheric effects. The six 20-m
101 reflectance imagery bands were resampled to 10-m using the bilinear resampling method (Berger et al., 2012). Any
102 poor-quality pixels, including clouds and shadows, were masked using the quality control band (QA60) and the cloud
103 probability product.

104 Sentinel-1 has a dual-polarization (VV and VH) C-band SAR instrument with a revisiting period of 6 days after
105 launching of Sentinel-1B (Torres et al., 2012). In this work, all Sentinel-1 imagery for 2023 were obtained through
106 the GEE platform, which have been preprocessed through radiometric calibration, thermal noise removal, and terrain
107 correction, and further resampled their resolution of 5 m × 20 m into 10 m × 10 m using Sentinel-1 Toolbox when
108 archived on the GEE platform.

109 Some previous works have demonstrated that topographical data can provide auxiliary and useful information in
110 land-cover mapping (Zhang et al., 2023b), currently, global 10 m digital elevation model (DEM) is not yet available.
111 In this work, we used the 30-m ASTER GDEM, which has low vertical error of 0.7 m (Tachikawa et al., 2011), to
112 obtained the elevation, slope, and aspect after bilinear resampling to 10 m × 10 m.

113 **2.2 Prior land-cover products**

114 **2.2.1 Impervious surface products**

115 Impervious surfaces are characterized by sparse spatial distribution and complicated spectral and spatial
116 heterogeneities; thus, it should be treated independently Its training samples are generated from five previous
117 products: 1) The Global 30-m Impervious Surface Dynamic (GISD30) dataset, developed with the combination of

118   spectral generalization and sample migration during 1985-2020 with the interval of 5-years, achieves a fulfilling
119   accuracy of 90.1% (Zhang et al., 2022). 2) The Global Impervious Surface Area (GISA 2.0) dataset, produced by
120   considering the inconsistency among four existing products, is an annual time-series impervious surface maps during
121   1985-2018 with the F1-score of 0.935 (Huang et al., 2022). 3) The 10 m impervious surface layer in ESA WorldCover
122   dataset was generated by the supervision classification from time-series Sentinel-1 and Sentinel-2 imagery (Zanaga
123   et al., 2021). It was demonstrated to achieve the great performance with producer's accuracy of 82.99% (Zhao et al.,
124   2023). 4) The impervious surface layer in ESRI Land Cover is developed from time-series Sentinel-2 imagery and
125   the deep-learning (Karra et al., 2021), and achieve high producer's accuracy of 88.42% (Zhao et al., 2023) .5) Global
126   urban boundary dataset (GUB) is generated by the combination of cellular-automata and morphological approach,
127   and shows a good agreement with the results from human interpretation (Li et al., 2020).

128   **Table 1**. The characteristics of prior land-cover products.

Category	Dataset name	Resolution	Year	Coverage	Reference
Impervious surface	GISD30	30	1985–2020	Global	Zhang et al. (2022)
	GISA 2.0	30	1985–2019	Global	Huang et al. (2022)
	Imp-ESA_LC	10	2021	Global	Zanaga et al. (2021)
	Imp-ESRI_LC	10	2023	Global	Karra et al. (2021)
	GUB	-	2020	Global	Li et al. (2020)
Wetland	GWL_FCS30D	30	2000–2022	Global	Zhang et al. (2024b)
	National Wetland Inventory	30	2019	United States	Wilen and Bates (1995)
	Global Mangrove Watch	30	1996–2020	Global	Bunting et al. (2022)
	Global tidal flat	30	2000–2022	Global	Zhang et al. (2023a)
	Global tidal marsh dataset	10	2020	Global	Worthington et al. (2024)
Land-cover	GLC_FCS30D	30	1985–2022	Global	Zhang et al. (2024c)
	Global oil palm dataset	30	1990–2021	Global	Descals et al. (2024)
	Global plantation map	30	1982–2020	Global	Du et al. (2022)

2.2.2 Wetland products

130   Because almost all global land-cover products have large uncertainties in wetlands identification (Zhang et al.,
131   2023b), wetlands should also be treated as independent land-cover type. The wetland training samples were also
132   derived from three existing wetland thematic products, including: 1) the GWL_FCS30D is an annual global wetland
133   products containing 8 wetland subcategories (5 inland and 3 coastal wetland subcategories), and achieves an overall
134   accuracy of 86.95 ± 0.44% (Zhang et al., 2024b). 2) The NWI (National Wetland Inventory) is national wetland
135   thematic products covering the whole United States and containing 8 wetland subcategories (Wilen and Bates, 1995).
136   3) The GMW (Global Mangrove Watch) and global tidal marsh products provide the spatial patterns of mangrove
137   and salt marsh with the overall accuracy of 87.4% and 85% (Bunting et al., 2022; Worthington et al., 2024).

2.2.3 GLC_FCS30D land-cover dynamic products

139   Except for wetlands and impervious surfaces, training samples for the remaining non-wetland natural land-cover
140   types are generated from the GLC_FCS30D dataset. It was developed from the combination of a continuous change
141   detection algorithm with an adaptive updating strategy and had 80.88% (±0.27%) accuracy covering the period of
142   1985–2022 with 35 fine land-cover subcategories. The dataset has high temporal stability in the European Union and
143   United States (Zhang et al., 2024c). In this work, we leverage this dynamic product to generate confident training
144   samples for non-wetland natural land covers, as described in the Section 3.1.

2.2.4 Tree-cover cropland datasets

146   It is noteworthy that the tree-cover cropland was only mapped in certain regions rather than globally in the
147   GLC_FCS30D (Zhang et al., 2021; Zhang et al., 2024c); thus, global oil palm and plantation datasets are also used
148   to identify tree-cover cropland. The global oil palm dataset is a time-series covering 1990–2020 and exceeds 91%
149   accuracy for industrial plantations and 71% accuracy for smallholders (Descals et al., 2024). A global plantation map
150   was generated by combining some prior global plantation products and the LandTrendr method, and has an F1 score
151   of 86.83% with ±5 years tolerance (Du et al., 2022).

3. Methodology

153   To achieve high quality with detailed categorizations in global 10-m land-cover mapping, a hierarchical land-
154   cover mapping methodology has been proposed. It leverages prior land-cover products and time-series satellite
155   observations. Figure 1 presents a flowchart of the proposed method, which involves four procedures: generating
156   hierarchical and globally distributed training samples from prior products, compositing multisource and
157   multitemporal training features from time-series Sentinel 1&2 imagery, hierarchical land-cover mapping using local
158   adaptive classifications, and accuracy assessment and cross-comparisons.
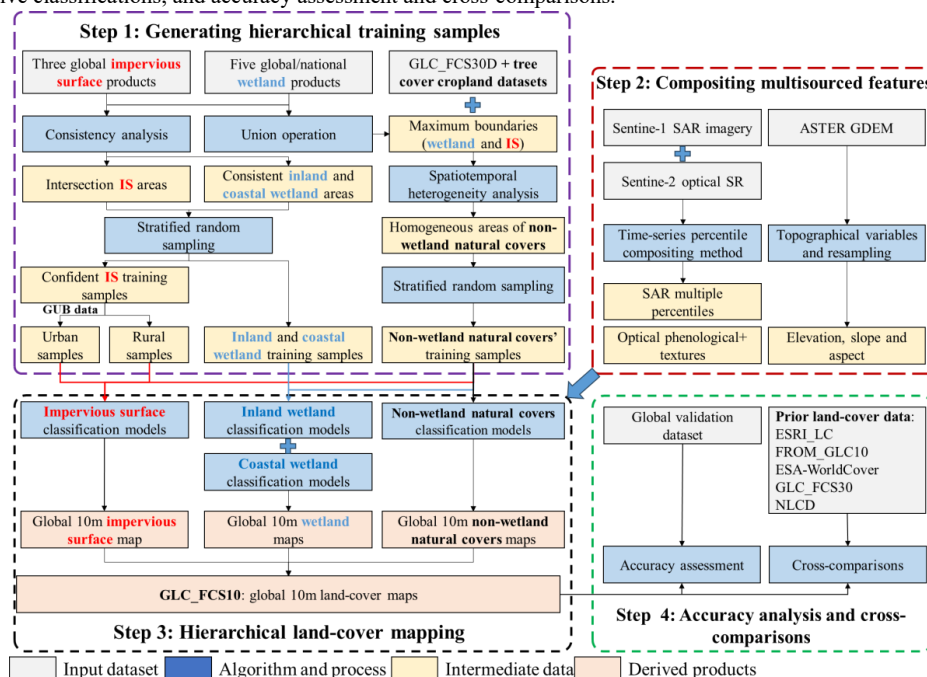
159
160   **Figure 1**. The flowchart of the proposed method for hierarchical land-cover mapping.

3.1 The description of the classification system

162   In this work, we develop a novel global 10-m land-cover dataset with a fine classification system (FCS). Table 2
163   presents the main characteristics of this FCS and its correspondence with the basic classification system. It contains
164   30 fine land-cover types and emphasizes the forest- and wetland-related subcategories, which are further subdivided
165   into 10 and 7 subcategories, respectively. The diversity of this fine classification system results from importing the
166   GWL_FCS30D (Zhang et al., 2024b) and GLC_FCS30D (Zhang et al., 2024c) products.

167   **Table 2**. The characteristics of the fine classification system in the GLC_FCS10.

Basic classification system	Fine classification system	Id

	Herbaceous rainfed cropland	11
Cropland	Tree or shrub covered rainfed cropland (orchard, oil palm…)	12
	Irrigated cropland	20
	Closed evergreen broadleaved forest	51
	Open evergreen broadleaved forest	52
	Closed deciduous broadleaved forest	61
	Open deciduous broadleaved forest	62
Forest	Closed evergreen needleleaved forest	71
	Open evergreen needleleaved forest	72
	Closed deciduous needleleaved forest	81
	Open deciduous needleleaved forest	82
	Closed mixed-leaf forest	91
	Open mixed-leaf forest	92
Shrubland	Evergreen shrubland	121
	Deciduous shrubland	122
Grassland	Grassland	130
Tundra	Lichens and mosses	140
	Swamp	181
	Marsh	182
	Lake/river flat	183
Wetland	Saline	184
	Mangrove forest	185
	Salt marsh	186
	Tidal flat	187
Impervious surfaces	Urban impervious surfaces	191
	Rural impervious surfaces	192
Bare areas	Sparse vegetation	150
	Bare areas	200
Water	Water	210
Permanent ice and snow	Permanent ice and snow	220

3.2 Generating hierarchical training samples

To ensure quality in global 10-m land-cover mapping, land surfaces are hierarchically divided into impervious surface, wetland, and non-wetland natural land-cover types. Their corresponding training samples also need to be generated independently. Because training sample quality greatly affects land-cover mapping performance (Foody and Arora, 2010; Zhang and Roy, 2017), generating confident and globally distributed training samples is a prerequisite for generating the GLC_FCS10.

3.2.1 Training areas of impervious surfaces

Regarding the training samples of impervious surfaces, we combine four prior global 10-m or 30-m impervious surface products (GISA 2.0, GISD30, Imp-ESA_LC, and Imp-ESRI_LC) and one urban boundary dataset (GUB) to automatically generate the training samples. Specifically, because the previous studies have demonstrated high-accuracies of three impervious surface products (Huang et al., 2022; Zanaga et al., 2021; Zhang et al., 2022)and high producer's accuracy of Imp-ESRI_LC (Zhao et al., 2023), the areas marked as impervious surfaces by all four products (GISD30-2020, GISA2.0-2019, Imp-ESA_LC-2021, and Imp-ESRI_LC-2023) are selected as candidate areas for generating the training samples (*TrainCanArea_imp*) in Eq. (1).

$$TrainCanArea_{imp} = GISD30 \cap GISA2.0 \cap (\text{Imp-ESA}_{LC}) \cap (\text{Imp-ESRI\_LC}) \qquad (1)$$

Afterward, we further consider the uneven distribution of rural and urban impervious surfaces as well as their spectral variability. If random sampling is used to obtain training samples from the *TrainCanArea_imp*, rural impervious surfaces are underrepresented due to their sparse distribution, thus, the GUB urban boundary dataset for 2020 is further used to divide the *TrainCanArea_imp* into urban (*TrainCanArea_urban*) and rural areas

186   (*TrainCanArea_rural*).

187   Beyond the confident impervious surface areas, it is equally important to identify high-quality natural land-cover

188   types (Zhang et al., 2024a). To avoid confusion between natural land-cover types and impervious surfaces, the

189   maximum impervious surface boundary (*MaxBound_imp*) is also generated. The training samples for natural land-

190   cover types should be located outside of the *MaxBound_imp*. To determine *MaxBound_imp*, the union of the four

191   products is applied as:

$$MaxBound_{imp} = GISD30 \cup GISA2.0 \cup (\text{Imp-ESA}_{LC}) \cup (\text{Imp-ESRI\_LC}) \qquad (2)$$

192 **3.2.2 Training areas of wetland**

193   In this work, wetlands are divided into four inland subcategories (swamp, marsh, river/lake flats, and saline) and

194   three coastal wetland subcategories (mangrove, salt marsh, and tidal flats in **Table 2**). Because coastal wetlands have

195   a more pronounced zonation, and the global coastal wetland mapping have make great progresses while the works of

196   global inland wetland mapping is still sparse (Wang et al., 2023), thus, the generation of wetland training candidate

197   areas further distinguishes between inland and coastal wetlands.

198   The time-series GWL_FCS30D wetland product covering the period of 2000–2022 is used to derive the inland

199   wetland training candidate areas (Zhang et al., 2024b). Because temporally stable areas achieve higher accuracy

200   (Yang and Huang, 2021), a temporally stable analysis is applied to the GWL_FCS30D, and only those stable areas

201   where wetland subcategories do not change during 2000–2022 are retained (yielding the training area,

202   *TrainCanArea_Inwet*). Then, because adjacent land-cover areas are easier to suffer from the higher misclassifications

203   (Radoux et al., 2014) and to the impact of the satellite geolocation error (Zhang and Roy, 2017), a spatial filter with

204   a local window of 3 pixels × 3 pixels is applied to *TrainCanArea_Inwet* to retain spatially homogeneous areas as the

205   training areas. Further, the integration of multiple wetland products improves sample quality, but there are few high-

206   quality wetland products that have been publicly shared. Only the National Wetland Inventory for 2019 is imported

207   to optimize the swamp and marsh land-cover types in *TrainCanArea_Inwet* over the United States. The areas

208   identified as swamp and marsh in *TrainCanArea_Inwet* and the National Wetland Inventory are retained. The

209   National Wetland Inventory does not identify river/lake flats or saline subcategories.

210   As for the three coastal wetland subcategories, their training areas are generated from the combination of

211   GWL_FCS30D and three coastal wetland products (GMW, GTF30, and GSM10 in **Table 1**). We identify temporally

212   stable coastal wetland areas from GWL_FCS30D, GMW, and GTF30 through time-series analysis and label them

213   GWL_stable, GMW_stable, and GTF_stable. Then, we intersect GWL_stable with GMW_stable to generate

214   mangrove forest training areas and intersect GWL_stable with GTF_stable to generate tidal flat training areas. Next,

215   as the GSM10 only provides salt marsh maps in 2020, the salt marsh training areas are selected as the intersection

216   between GWL_stable and GSM10. The mangrove forest, tidal flat, and salt marsh training areas are grouped as

217   *TrainCanArea_Cowet*.

218   Last, the maximum wetland boundary ($MaxBound_{wet}$) is also necessary for the subsequent identification of

219   training areas for non-wetland natural land-cover types. $MaxBound_{wet}$ is determined as the union of the five global

220   wetland products:

$$MaxBound_{wet} = GWL\_FCS30D \cup \text{NWI} \cup GMW \cup GTF30 \cup GSM10 \qquad (3)$$

221 **3.2.3 Training areas of non-wetland natural land-covers**

222   Many previous works have emphasized that these spatiotemporally stable areas always performed higher

223   mapping accuracy (Zhang and Roy, 2017; Zhang et al., 2024c). In this work, the time-series global 30-m land-cover

224   dynamic product (GLC_FCS30D), covering the period of 1985–2022 is used. The product uses a classification system

225   like the one used in this work. Specifically, three measures are taken to identify spatiotemporally stable areas of non-

226   wetland natural land-cover types from GLC_FCS30D: 1) A time-series consistency analysis is applied to the
227   GLC_FCS30D, and only stable areas during 1985–2022 will be retained as *TrainCanArea_NLCs*. 2) The
228    $MaxBound_{imp}$ and $MaxBound_{wet}$ are imported to mask the *TrainCanArea_NLCs*, i.e., the training areas for non-
229   wetland natural land-cover types should be located outside of $MaxBound_{imp}$ and $MaxBound_{wet}$. The aim of this
230   step is to minimize confusion between non-wetland natural land-cover types and two other land-cover types. 3) A
231   morphological erosion filter with a local window of 3 pixels × 3 pixels is used to find the spatially homogeneous
232   areas for non-wetland natural land-cover types.
233   As mentioned in Section 2.2.4, the training areas for tree-cover cropland (oil palm, orchards, etc.) from the
234   GLC_FCS30D do not cover the globe. These training areas are therefore divided into herbaceous rainfed cropland
235   and tree- or shrub-cover cropland. Because the global oil palm and global plantation datasets provide the plantation
236   years of oil palm and orchards at 30 m, we overlap the training areas of rainfed cropland, oil palm, and orchard
237   plantation from the global plantation dataset to extract the training areas for tree-cover cropland. Then, to minimize
238   error, the tree-cover cropland training areas are further filtered using a local window of 3 pixels × 3 pixels to ensure
239   spatial homogeneity of tree-cover cropland training areas.

240   **3.2.4 Generating a globally distributed training pool from stratified sampling**
241   Although we take a series of measures to ensure training area quality (including: *TrainCanArea_urban,*
242   *TrainCanArea_rural, TrainCanArea_Inwet, TrainCanArea_Cowet,* and *TrainCanArea_NLCs*), how to generate
243   training samples from the training areas needs to address the following two aspects.
244   First, the distribution and balance of training samples greatly affect the subsequent land-cover classification
245   ([Ghorbanian et al., 2020](#); [Jin et al., 2014](#); [Mellor et al., 2015](#); [Pelletier et al., 2017](#); [Zhu et al., 2016](#)). There are two
246   options to allocate the sample distribution: equal or area-fraction allocation ([Zhang et al., 2021](#)). Equal distribution
247   means that all land-cover types have the same number of training samples, i.e., the sample sizes of sparse land covers
248   will be augmented while those of the abundant land covers will be suppressed. In contrast, area-fraction distribution
249   allocates the sample size according to the land-cover area of each type, that is, abundant land covers have larger
250   sample sizes while sparse land-cover types have smaller sample sizes ([Zhu et al., 2016](#)). Because impervious surfaces
251   and wetlands are sparser than natural land-cover types and are independently generated, equal-distribution allocation
252   is suitable to enhance the training samples' ability to characterize these two land-cover types. As for the non-wetland
253   natural land-covers, the area-fraction allocation is more appropriate for the non-wetland natural land-cover types
254   because we want to optimize results for all non-wetland natural land-cover types rather than a single land-cover type.
255   Meanwhile, to avoid sample size imbalance in the area-fraction allocation, maximum and minimum sample sizes of
256   8000 pixels and 600 pixels are chosen for the abundant and sparse land-cover types, respectively (suggested by the
257   work of [Zhu et al. (2016)](#)).
258   Second, most high-quality training samples (except for those for impervious surfaces) are derived from the 30-
259   m training areas, so there is also a need to reduce the 30-m training samples to 10-m samples to achieve a global 10-
260   m land-cover map. In this work, the metric centroid method is adopted, which had been used to downscale 500-m
261   training samples from MCD12Q1 to 30-m in the work of [Zhang and Roy (2017)](#). Specifically, as each 30-m pixel
262   corresponds to 3 × 3 10-m pixels, we first find the centroid from these nine pixels as $P_{centroid}$ through spectral
263   averaging, and then the point with the smallest absolute distance with $P_{centroid}$ was chosen as the optimal downscaled
264   10-m sample point [**Eq. (4)**].

$$P_i = \underset{i}{\arg\min}\left(\left|\boldsymbol{\rho}_{P_i} - \boldsymbol{\rho}_{P_{centroid}}\right|\right), \boldsymbol{\rho}_{P_{centroid}} = \frac{1}{9}\sum_{j=1}^{9}\frac{\boldsymbol{\rho}_{P_j}}{9} \tag{4}$$

265   Where $\boldsymbol{\rho}_{P_i}$ is the spectra value of composited Sentinel-2 training features (See Section 3.3) at pixel P_i. If more than
266   one point in the nine pixels has the same minimum absolute distance, then we pick randomly from among them.

3.3 Compositing multisourced training features

In addition to high-confidence training samples, how to generate these multisource training features is also important (Dong et al., 2015; Yang and Huang, 2021). In this work, we composite multitemporal optical and SAR information from Sentinel-1 and Sentinel-2 time-series observations. First, because of the overlapping orbits of the satellites and the effects of clouds and shadows, there are substantial differences in the clear-sky observations in different regions. Compositing methods help to obtain dimensionally consistent spectral-phenological features. The percentile-based statistical multitemporal compositing method attracts attention because of its robustness, efficiency, and simplicity (Azzari and Lobell, 2017). This method rearranges intra-annual time-series reflectance according to mathematical magnitude and take the corresponding quartiles to reflect the phenological variation of the time-series (Hansen et al., 2014). Thus, in percentile-based compositing, time-series Sentinel-2 images are composited into the 10th, 30th, 50th, 70th, and 90th percentiles for their 10 optical bands from visible to shortwave infrared and three typical indexes [NDVI, NDWI, and LSWI in **Eq. (5)**]. The 10th and 90th percentiles are selected to represent the poles of time-series variations and also suppress the effects of residual cloud and shadow, and the other three percentiles can partly reflect the phenological variations (Xie et al., 2020). Meanwhile, another major advantage of 10-m Sentinel-2 imagery is that it provides clearer textural features, so we generate time-series texture features from the five percentiles in the NIR bands using the gray level co-occurrence matrix. Only the texture features in the NIR band are extracted to avoid redundancy, because of the texture similarity within different spectral bands (Rodriguez-Galiano et al., 2012).

$$NDVI = \frac{\rho_{NIR} - \rho_{r}}{\rho_{NIR} + \rho_{r}}, LSWI = \frac{\rho_{NIR} - \rho_{SWIR1}}{\rho_{NIR} + \rho_{SWIR1}} \text{ and } NBWI = \frac{\rho_{green} - \rho_{SWIR1}}{\rho_{green} + \rho_{SWIR1}} \tag{5}$$

where $\rho_{green}, \rho_{r}, \rho_{NIR}, \rho_{SWIR1}$ are the spectral bands of green, red, NIR, and SWIR1 in the Sentinel-2 imagery.

Then, because SAR signals are sensitive to changes in surface water dynamics and spatial structure, it is also necessary to extract multitemporal SAR features from Sentinel-1 imagery (Bullock et al., 2022; Dabrowska-Zielinska et al., 2018; Zhang et al., 2020). The percentile-based composited method is also used to capture the time-series variabilities of VV and VH at the 10th, 30th, 50th, 70th, and 90th percentiles. In summary, a total of 10 SAR features are composited from time-series Sentinel-1 observations.

Afterward, because some land-cover types are characterized by important topographic distribution (e.g., permanent snow and ice are clustered in high elevation areas, croplands and impervious surfaces usually locate on these flat areas), the topographical variables (slope, aspect and elevation), generated from the resampled ASTER GDEM dataset, are collected into the multisourced training features. It should be noted that some 5 ×5 geographical tiles do not have sufficient Sentinel-1 observational data in 2023 since Sentinel-1B is retired in 2022, the corresponding tiles use only Sentinel-2 and topographic data.

3.4 Hierarchical land-cover mapping

A major advantage of hierarchical land-cover mapping is the ability to improve the characterization of complex land-covers with independent models. In this work, we first separate global land-cover types into impervious surfaces and natural land-cover types, then identify the wetlands from among the natural land-covers, and finally classify the remaining non-wetland natural land-cover types into 20 land-cover subcategories.

3.4.1 The separation of impervious surfaces and natural surfaces

To separate impervious surfaces and natural surfaces, we rely on the globally distributed training samples (Section 3.2.4) and the combination of multitemporal optical and SAR features. Specifically, because we divide impervious surfaces training samples into rural and urban samples and design the equal distribution to enhance the training samples' ability to characterize impervious surfaces. The ratio of urban samples, rural samples, and natural surfaces is 1:1:1 for each 5 × 5 geographical tile. We split the globe into 984 5 ×5 geographical tiles, because some

308 studies emphasized that the local adaptive modeling usually achieves better mapping accuracy than single land-cover
309 global modeling (Zhang et al., 2021). Then, when building the training model for each 5 × 5 geographical tile, we
310 also import training samples within their spatial neighborhood of 3 × 3 tiles to ensure spatial consistency over the
311 adjacent tiles. Afterward, we can produce 984 5 ×5 impervious surface and natural land cover maps using the local
312 adaptive modeling strategy. In addition, although we divide the training samples into urban and rural samples, there
313 is serious confusion between urban and rural areas in the classification maps because they share similar spectral and
314 SAR characteristics. We therefore consider the two subcategories to be inseparable at the classification stage.
315 Correspondingly, inspired by the work of Li et al. (2020) who used the cellular automata and morphological
316 approaches to accurately capture urban boundaries, this method is also applied in this work to distinguish urban and
317 rural impervious surfaces.

318   The random forest classification model (including the later section 3.4.2 and 3.4.3) is selected. The random
319 forest has some advantages over other traditional classifiers, such as managing high-dimensional data more efficiently,
320 having higher robustness, being insensitive to parameter settings, and avoiding overfitting problems effectively
321 (Belgiu and Drăguţ, 2016; Breiman, 2001). In terms of its parameter settings, the random forest only has two
322 adjustable parameters, and the variations of these two parameters have little effect on the performance of the random
323 forest model (Du et al., 2015; Gislason et al., 2006), thus, the default parameter settings are applied to train the
324 random forest models on the GEE platform.

3.4.2 The separation of wetland and non-wetland natural land-cover types

326   In terms of how to identify the fine wetland subcategories from natural land-covers, we use the stratified wetland
327 mapping algorithm to independently distinguish coastal wetlands and inland wetlands. Wetlands are divided into four
328 inland and three coastal wetland subcategories (in **Table 2**), and equal-distribution sampling is used to enhance the
329 training samples' ability to characterize wetlands. The approximate ratio of inland wetlands, coastal wetlands, and
330 non-wetlands (including water body, forest, grassland, bare land, and others) is 4:3:5 in areas where they coexist.
331 Then, because coastal wetlands have a more pronounced zonation, we can obtain their maximum coverage through
332 the union of some previous coastal wetland products, as Eq. (6).

$$MaxBound_{Cos\_wet} = GWL\_FCS30D\_Coastal \cup GMW \cup GTF30 \cup GSM10 \qquad (6)$$

333 When building the wetland random forest classification models for each 5 ×5 geographical tile, we first train the
334 coastal wetland classification model using the coastal wetland and non-wetland training samples within their spatial
335 neighborhood of 3 × 3 tiles, and combine multisourced training features to identify the spatial distribution of coastal
336 wetlands within the $MaxBound_{Cwet}$; i.e., all coastal wetland pixels should be within the $MaxBound_{Cwet}$, otherwise,
337 they would be corrected.

338   Afterward, the inland wetland and non-wetland training samples are used to train another random forest
339 classification model, and the remaining natural land-cover types are further classified as four inland wetland
340 subcategories and non-wetland natural land-cover types using the inland wetland classification model.

3.4.3 Mapping of non-wetland natural land-cover types

342   After classifying the impervious surface and wetlands using the hierarchical land-cover mapping, we now need
343 to classify the remaining non-wetland natural land-cover types. Like the previous mapping processes, the local
344 adaptive random forest models are trained for each 5 ×5 geographical tile using the corresponding training samples
345 within the spatial neighborhood of 3 × 3 tiles. The non-wetland natural land-cover types are classified through a
346 combination of trained random forest models and multisource training features. Lastly, after overlapping the
347 hierarchical maps for impervious surface, wetland, and non-wetland natural land-cover types, we can obtain 10-m
348 land-cover maps with a fine classification system.

3.5 Accuracy assessment and cross-comparison

To comprehensively assess the performance of our developed GLC_FCS10 products, a globally distributed validation dataset and one third-party validation dataset are collected to quantify the accuracy metrics. First, the global validation dataset, guided by the work of (Zhao et al. (2023), is collected through stratified random sampling and visual interpretation from high-resolution remote sensing imagery in 2023. Figure 2 illustrates the spatial distribution of the global validation dataset; it contains 56121 globally distributed validation points and covers 16 land-cover types. Next, the Land Cover Monitoring, Assessment, and Projection Collection (LCMAP) validation dataset (called LCMAP_V), as a national third-party validation dataset, contains 16082 nationally distributed validation points during 1985–2021 (Stehman et al., 2021). In this work, the LCMAP_Val in 2021 is also updated to 2023 through visual interpretation. Afterward, the confusion matrix and four accuracy metrics are calculated, including: the overall accuracy (O.A.) and kappa coefficient (measuring the comprehensive performance) and the producer accuracy (P.A.), and the user accuracy (U.A.), which measure the commission and omission errors for each land-cover type to quantify the accuracy of GLC_FCS10 (Foody and Arora, 2010; Liu et al., 2007; Nelson et al., 2021).
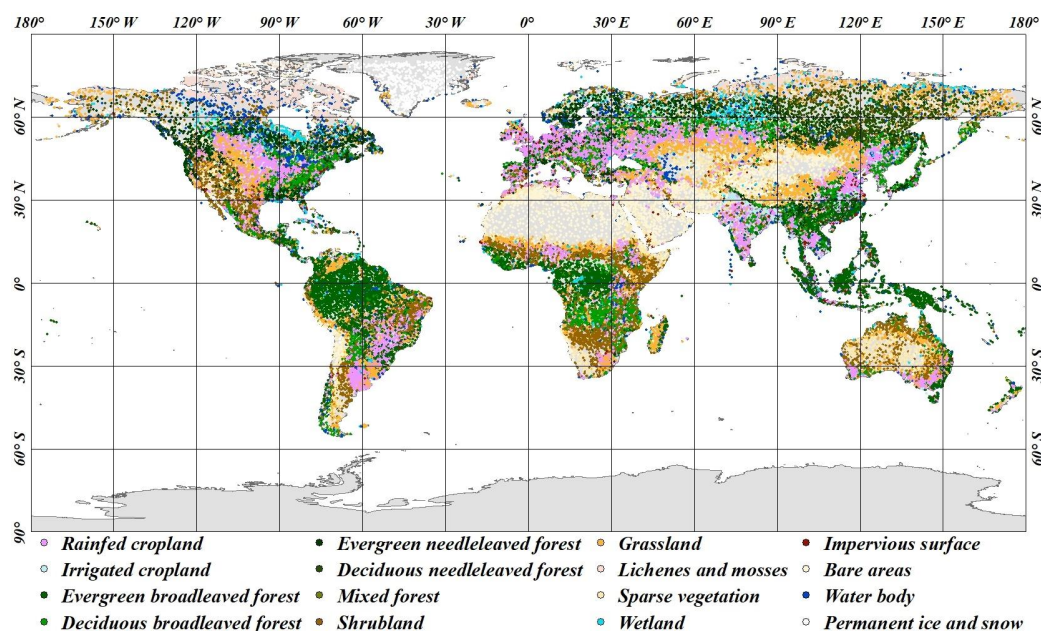
Figure 2. The spatial distribution of global validation samples containing 16 land-cover types in 2023.

In addition, to qualitatively investigate the performance of GLC_FCS10, three global 10-m land-cover products [ESRI_LC (Karra et al., 2021), ESA WorldCover (Zanaga et al., 2021), and FROM_GLC10 (Gong et al., 2019)], and one 30-m land-cover product [GLC_FCS30 (Zhang et al., 2021)] are collected as comparative products. None of these five data products have been updated to 2023. Their latest available data will be collected for our comparative analysis.

4. Results and discussions

4.1 Overview of the GLC_FCS10 maps

Figure 3 illustrates the spatial distribution of the GLC_FCS10 land-cover maps with 30 fine land-cover types in 2023. Overall, it accuratersizes global land-cover patterns, i.e., forests concentrate in tropical rainforest

374   regions and cold temperate forest zones in the northern hemisphere, cropland is found in low-lying plains areas such
375   as the North China Plain, Central Plains of the United States, Central Eurasia, and bare land and grassland are
376   distributed in arid and semiarid areas. Meanwhile, because a characteristic of the GLC_FCS10 is its diverse
377   classification system, we can see that broadleaved forests are found in low- and medium-altitude regions, while
378   needle-leaved forests are distributed in cold temperate zones as well as in high-altitude areas.

379
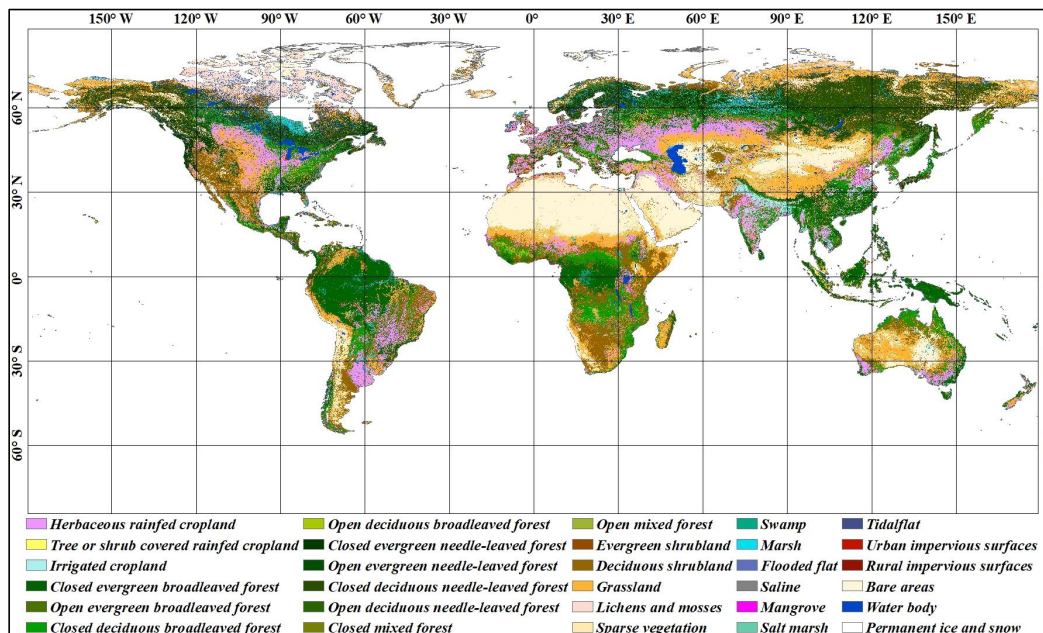
380   **Figure 3**. Spatial distribution of the 30 fine land-cover types in GLC_FCS10 land-cover maps in 2023.

381   **4.2 Accuracy assessment**

382   **4.2.1 Global-scale accuracy assessment**

383   Table 3 presents the confusion matrix between GLC_FCS10 and the 56121 globally distributed validation points
384   for 10 major land-cover types (corresponding to the basic classification system in Table 2). Overall, GLC_FCS10
385   achieves an O.A. of 83.16% and a kappa coefficient of 0.789. For specific land-cover types, permanent snow and ice,
386   water bodies, forest, impervious surfaces, and cropland perform the best, with the corresponding U.A. and P.A. values
387   approximating or exceeding 90%. Their high accuracies stem from the distinct spectral properties inherent to water
388   bodies and permanent ice and snow, the abundant coverage of cropland and forest, and hierarchical land-cover
389   mapping for impervious surfaces. However, shrubland, grassland, tundra, and wetlands suffer obvious
390   misclassifications, in which the shrubland has the lowest U.A. of 67.04% and wetland has the lowest P.A. of 53.69%.
391   There are considerable confusions between shrubland, grassland, and bare areas because they share similar spectral
392   characteristics and coexist in arid and semiarid areas. Wetlands have the lowest P.A. due to the confusions between
393   wetlands, water bodies, forest, and grassland. Wetlands have complicated and heterogeneous spectral and temporal
394   variations, thus, the swamp subcategory is easily confused with forest, and the marsh subcategory shares spectral
395   characteristics with grasslands (Zhang et al. (2023b).

396   **Table 3**. The confusion matrix between GLC_FCS10 and the globally distributed validation dataset for 10 major
397   land-cover types.

	Crop	Forest	Shrub	Grass	Tundra	Wetland	Impervious	Barren	Water	Ice-Snow	Total	U.A.
Crop	8442	339	588	768	0	53	39	46	9	0	10284	82.09
Forest	161	18342	1191	189	0	250	2	12	4	0	20151	91.02
Shrub	190	701	4091	922	12	72	4	109	1	0	6102	67.04
Grass	673	255	275	5817	33	170	7	391	4	1	7626	76.28
Tundra	0	25	78	153	805	2	0	61	0	0	1124	71.62
Wetland	10	74	136	100	14	946	1	23	30	0	1334	70.91
Impervious	20	6	11	28	0	1	902	5	0	0	973	92.70
Barren	66	5	187	544	24	29	6	3882	3	13	4759	81.57
Water	2	6	9	4	0	239	1	25	2328	0	2614	89.06
Ice-Snow	0	1	1	33	0	0	0	5	1	1113	1154	96.45
Total	9564	19754	6567	8558	888	1762	962	4559	2380	1127	56121	
P.A.	88.27	92.85	62.30	67.97	90.65	53.69	93.76	85.15	97.82	98.76		
O.A.						83.16						
Kappa						0.789						

398   To intuitively understand the spatial distribution of the GLC_FCS10 accuracy metrics, Fig. 4 presents the spatial
399 variations of O.A. and the kappa coefficient among 30 climate zones from Köppen climate zones. There is high
400 consistency of the O.A. and kappa coefficient within the spatial patterns, i.e., some climatic transition zones, land-
401 cover heterogeneity zones, cloud-contaminated tropical zones, and small subdivisions tend to have lower accuracy
402 (below 80%). Conversely, some homogeneous zones (such as Greenland and the Sahara Desert) and forest- or
403 cropland-rich zones (such as the east-central United States, central Eurasia, and East Asia) achieve the high O.A. and
404 kappa coefficient.

405
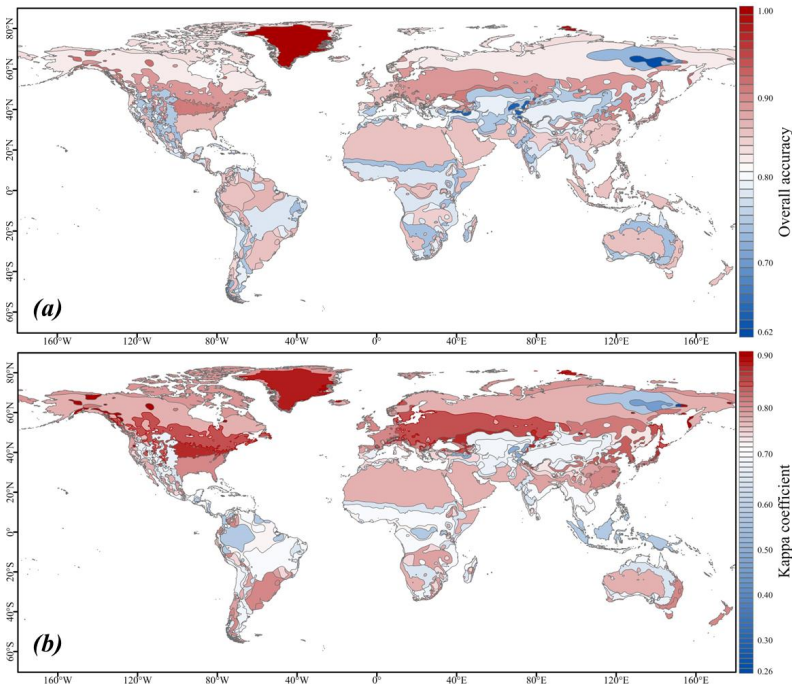
406 **Figure 4**. (a) Regional O.A. and (b) kappa coefficient of the GLC_FCS10 land-cover maps among various Köppen
407 climate zones (http://koeppen-geiger.vu-wien.ac.at/) using the globally distributed validation points.

408   Table 4 further analyzes the confusion matrix between GLC_FCS10 and the global validation dataset with 16
409   land-cover types (refining the forest and cropland subcategories). Under this fine classification system, the
410   GLC_FCS10 achieves an O.A. of 76.45% and a kappa coefficient of 0.736, which are reduced by 6.71% and 0.053,
411   respectively, from the metrics in Table 3. This reduction is due to confusion between the finer land-cover
412   subcategories; e.g., forests have a U.A. value of 91.02% in Table 3, but when broken down into five forest
413   subcategories the average U.A. value drops to 68.52%. Taking mixed forest as an example, it has a low accuracy of
414   only 44.17%, of which the proportions misclassified as evergreen broadleaved forest (EBF), deciduous broadleaved
415   forest (DBF), evergreen needleleaved forest (ENF), and deciduous needleleaved forest (DNF) are 5.34%, 7.77%,
416   27.18%, and 5.83%, respectively. Higher likelihoods of confusion exist for closely related land-cover subcategories;
417   e.g., the highest proportion of misclassification in EBF is in DBF, and rainfed cropland is easily misclassified as
418   irrigated cropland, shrubland, or grassland. Previous research also demonstrated that considerable misclassifications
419   occur between similar land-cover types (Homer et al., 2020; Wickham et al., 2021; Zhang et al., 2021; Zhang et al.,
420   2024c).

421   **Table 4**. The confusion matrix between GLC_FCS10 and the globally distributed validation dataset for 16 land-cover
422   types.

	RCP	ICP	EBF	DBF	ENF	DNF	MF	SHB	GRS	LMS	SPV	WET	IMP	BAL	WTR	SNW	Total	U.A.
RCP	7575	302	134	137	21	13	6	574	746	0	10	24	31	35	6	0	9614	78.79
ICP	121	444	19	7	2	0	0	14	22	0	1	29	8	0	3	0	670	66.27
EBF	138	0	7263	842	289	59	48	429	70	0	0	140	1	1	2	0	9282	78.25
DBF	21	1	375	3955	235	149	61	482	52	0	0	40	0	1	0	0	5372	73.62
ENF	0	0	191	129	2535	533	11	138	28	0	0	51	1	3	1	0	3621	70.01
DNF	1	0	0	77	122	1278	4	127	37	0	1	16	0	6	1	0	1670	76.53
MF	0	0	11	16	56	12	91	15	2	0	0	3	0	0	0	0	206	44.17
SHB	184	6	60	440	52	140	9	4091	922	12	40	72	4	69	1	0	6102	67.04
GRS	654	19	24	109	21	98	3	275	5817	33	232	170	7	159	4	1	7626	76.28
LMS	0	0	0	6	1	18	0	78	153	805	18	2	0	43	0	0	1124	71.62
SPV	40	3	0	2	1	2	0	0	0	11	266	6	1	0	1	3	336	79.17
WET	8	2	29	9	9	27	0	136	100	14	12	946	1	11	30	0	1334	70.91
IMP	14	6	4	1	0	1	0	11	28	0	0	1	902	5	0	0	973	92.70
BAL	20	3	0	0	0	0	0	187	544	13	118	23	5	3498	2	10	4423	79.09
WTR	2	0	1	1	1	1	2	9	4	0	0	239	1	25	2328	0	2614	89.06
SNW	0	0	0	1	0	0	0	1	33	0	0	0	0	5	1	1113	1154	96.45
Total	8778	786	8111	5732	3345	2331	235	6567	8558	888	698	1762	962	3861	2380	1127	56121	
P.A.	86.30	56.49	89.55	69.00	75.78	54.83	38.72	62.30	67.97	90.65	38.11	53.69	93.76	90.60	97.82	98.76		
O.A.									76.45									
Kappa									0.736									

423
424   **Note**: RCP: rainfed cropland, ICP: irrigated cropland, EBF: evergreen broadleaved forest, DBF: deciduous broadleaved forest, ENF: evergreen needleleaved forest,
425   DNF: deciduous needleleaved forest, MF: mixed forest, SHB: shrubland, GRS: grassland, LMS: lichens and mosses, SPV: sparse vegetation, WET: wetland, IMP:
       impervious surface, BAL: bare areas, WTR: water body, SNW: permanent ice and snow

426   **4.2.2 National-scale accuracy analysis using the LCMAP_Val datasets**

427   Table 5 presents the confusion matrix for GLC_FCS10 based on the LCMAP_Val validation points over the
428   America. It should be noted that the LCMAP_Val dataset only contains eight land-cover types and merges shrubland
429   and grassland into one mosaiced land-cover type (grass/shrub). The GLC_FCS10 achieves O.A. of 85.09% and a
430   kappa coefficient of 0.804 using these 16082 national validation points. Regarding the U.A. and P.A., the cropland,
431   forest, water. and grass/shrub land-cover types achieve balanced U.A. and P.A. values approximating or exceeding
432   80%. In contrast, developed land has the lowest U.A. of 54.26% with high P.A. of 98.85%, mainly because of the

433 difference in definitions of developed land and impervious surfaces. The LCMAP_Val definition of developed land
434 is broad enough to classify inner-city greenery as developed land as well (Xian et al., 2022), which is considered a
435 vegetation land-cover type in the GLC_FCS10. Barren land has the lowest P.A. value of 31.93%, indicating a high
436 commission error of 68.07%. Most of these misclassifications came from the confusion between barren land and
437 grass/shrub land-cover types. It is noteworthy that the grass/shrub shares similar spectral characteristics with barren,
438 and both of them co-exist in arid regions of the western United States, thus, it is usually difficult to distinguish
439 between the two with high accuracy.

440 **Table 5.** The confusion matrix between GLC_FCS10 and the LCMAP_Val dataset.

	Cropland	Forest	Grass/Shrub	Wetland	Developed	Barren	Water	Ice & Snow	Total	U.A.
Cropland	3445	28	393	6	0	9	2	0	3883	88.72
Forest	7	4621	133	92	0	0	2	0	4855	95.18
Grass/Shrub	368	358	3440	21	1	272	1	0	4461	77.11
Wetland	37	260	30	522	1	0	5	0	855	61.05
Developed	44	69	164	3	344	9	1	0	634	54.26
Barren	1	0	0	10	0	137	1	0	149	91.95
Water	0	2	1	63	2	1	1173	0	1242	94.44
Ice & Snow	0	0	0	0	0	1	0	2	3	66.67
Total	3902	5338	4161	717	348	429	1185	2	16082	
P.A.	88.29	86.57	82.67	72.80	98.85	31.93	98.99	100.00		
O.A.					85.09					
Kappa					0.804					

441 Figure 5 illustrates the spatial distribution of O.A. and kappa coefficient values among different Köppen climate
442 zones using the LCMAP_Val validation points over the America. There is notable consistency between O.A. and
443 kappa coefficient in terms of the spatial patterns, i.e., the GLC_FCS10 considerably outperforms the Western U.S. in
444 the Eastern U.S. and has an optimal kappa coefficient of more than 0.8 in the Northeastern U.S. Combined with the
445 climatic distribution, it performs relatively poorly in the arid and semi-arid zones of the Midwestern U.S., mainly
446 attributed to the difficulty in distinguishing between shrubs, grasses, and bare land within the region.
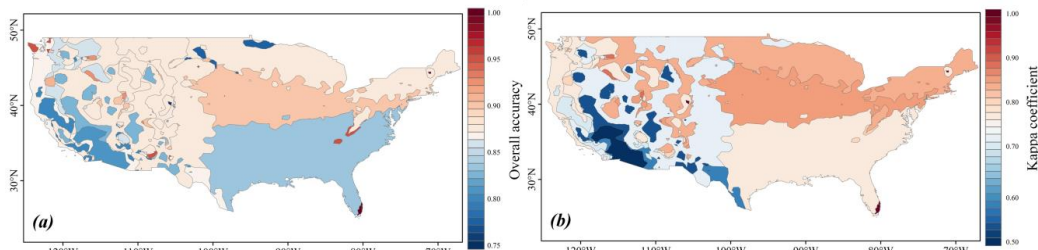
447
448 **Figure 5.** The spatial distributions of (a) O.A. and (b) kappa coefficient using the LCMAP_Val validation points over
449 the America among various Köppen climate zones.

450 **4.3 Cross-comparisons with previous land-cover products**

451 Table 6 gives quantitative comparisons among GLC_FCS10 and four public global 10- or 30-m land-cover
452 products using the LCMAP_Val dataset. The GLC_FCS10 achieves the highest O.A. of 85.09% and a kappa
453 coefficient of 0.804, followed by the ESA WorldCover (82.34% and 0.760) and ESRI_LC (82.10% and 0.754), while
454 the GLC_FCS30 and FROM_GLC10 have relatively inferior performance, below 80%. Specifically, in terms of the
455 P.A., U.A. and F1-score, we can find that: 1) all five products achieve superior performance for water with

456   corresponding P.A., U.A. and F1 score values of more than 90%. 2)The GLC_FCS10 and ESA WorldCover have

457   advantages over other products for cropland and forest (with F1 scores exceeding 85%). The ESRI_LC F1 scores for

458   cropland, forest, and grass/shrub exceed 80%. 3)All five products faced challenges for wetlands and barren land due

459   to their complicated spectral characteristics. Taking wetlands as an example, the GLC_FCS10 achieves the highest

460   F1 score of 66.63%, with most other products below 50%. The FROM_GLC10 has the lowest F1 score of 7.58%. 4)

461   As stated in Section 4.2.2, the difference in definitions for developed land and impervious surfaces mean that all

462   land-cover products have lower U.A. than P.A. values for developed land, i.e., they cannot identify inner-city greenery

463   as impervious surfaces.

464   **Table 6.** Comparisons among GLC_FCS10 and four other comparative products using the LCMAP_Val dataset.

		Cropland	Forest	Grass/Shrub	Wetland	Developed	Barren	Water	Snow	O.A.	Kappa
GLC_FCS10	U.A.	88.72	95.18	77.11	61.05	54.26	91.95	94.44	66.67		
	P.A.	88.29	86.57	82.67	72.80	98.85	31.93	98.99	100.0	85.09	0.804
	F1	88.50	90.67	79.79	66.41	70.06	47.40	96.66	80.00		
FROM_GLC10	U.A.	71.14	87.13	73.70	4.02	41.64	90.50	96.03	100.0		
	P.A.	89.17	82.42	73.47	66.00	85.31	9.30	98.34	50.00	74.31	0.653
	F1	79.14	84.71	73.58	7.58	55.96	16.87	97.17	66.67		
ESA WorldCover	U.A.	86.14	94.51	80.69	13.78	35.49	93.85	97.41	100.0		
	P.A.	93.09	82.00	85.15	88.28	97.20	14.38	98.93	75.00	82.34	0.760
	F1	89.48	87.81	82.86	23.84	52.00	24.94	98.16	85.71		
ESRI_LC	U.A.	90.02	82.84	84.98	10.15	69.36	56.52	97.69	100.0		
	P.A.	80.65	83.05	81.86	69.72	74.38	38.72	98.48	25.00	82.10	0.754
	F1	85.08	82.94	83.39	17.72	71.78	45.96	98.08	40.00		
GLC_FCS30	U.A.	85.78	88.85	75.29	37.68	38.10	73.49	90.79	100.0		
	P.A.	77.39	74.69	84.47	56.09	91.70	20.08	98.14	75.00	77.76	0.699
	F1	81.37	81.16	79.62	45.08	53.83	31.54	94.32	85.71		

465   Figure 6 compares GLC_FCS10 with ESA WorldCover, ESRI_LC, GLC_FCS30, and FROM_GLC10 on the

466   East Coast of the United States. Overall, there is the highest consistency between GLC_FCS10 and actual land-cover

467   situations, i.e., wetlands are predominantly found in low-lying river valleys and along the coast, and with a cross-

468   section of forests and cropland due to the undulating topography. Conversely, ESA WorldCover has the largest forest

469   area because some swamps or woody wetlands are labeled as forests (Fig. 6R1 is an enlargement showing an

470   example). ESA WorldCover also has the smallest impervious surface area because some is misclassified as forest

471   (Fig. 6R2 is an enlargement showing an example). Thus, ESA WorldCover has low U.A. values of 13.78% and 35.49%

472   for wetland and developed land, respectively (Table 6). ESRI_LC has the largest impervious surface area and also

473   identifies some swamps as forest, so it has the lowest P.A. value of 74.38% for developed land. ESRI_LC

474   overestimates impervious surfaces and has obvious omission errors for swamps. FROM_GLC10 has the lowest

475   wetland area, i.e., some swamps are classified as forest and herbaceous wetlands are labeled as water, so it has the

476   lowest U.A. value of 4.02% for wetlands in Table 6. Last, GLC_FCS30 also has omission errors for wetlands (the

477   red rectangle on GLC_FCS30) and lacks spatial details for some small objects (such as small rivers in Fig. 6R1).

478
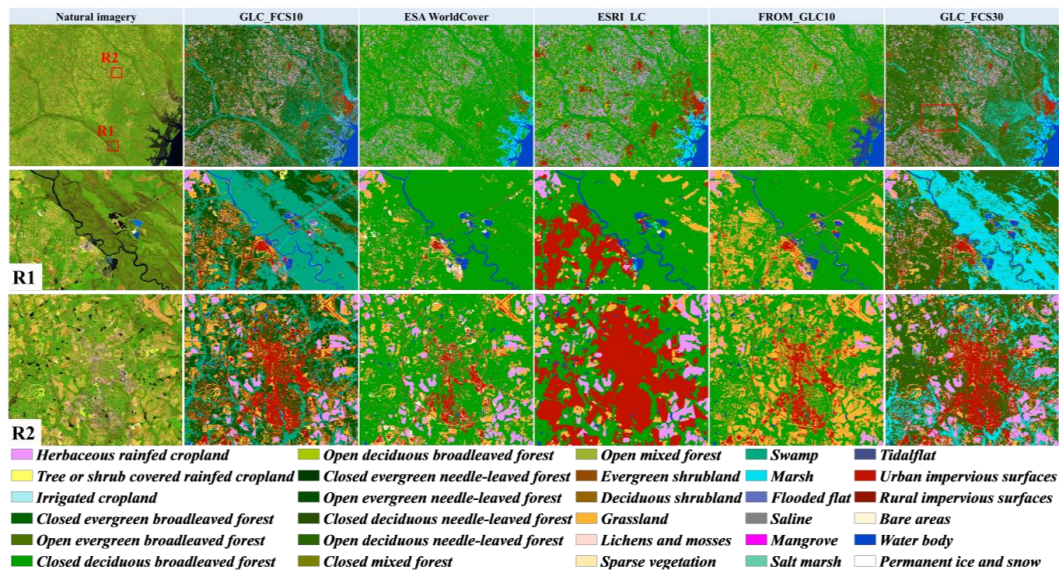
479 **Figure 6**. Comparisons among GLC_FCS10 and ESA WorldCover, ESRI_LC, GLC_FCS30, and FROM_GLC10 on

480 the East Coast of the United States. Images in the first column are false-color composited from time-series Sentinel-

481 2 imagery.

482   Figure 7 presents comparisons for the moddle reaches of the Yangtze River, China. All land-cover products

483 accurately capture the regional spatial patterns, and GLC_FCS10 and GLC_FCS30 have advantages with the

484 diversity of land-cover types over the other three products. Specifically, Fig. 7R1 illustrates cross-comparisons for

485 the megacity of Wuhan. ESA WorldCover underestimates and has the lowest impervious surface area, ESRI_LC

486 overestimates and has the highest impervious surface area, and FROM_GLC10 misclassifies some impervious

487 surfaces as grassland (Huang et al., 2022).. Based on the former comparison and previous works (Huang et al., 2022),

488 the ESA WorldCover underestimates these low-density impervious surfaces, the ESRI_LC suffers the overestimation

489 problem on the impervious surfaces, and FROM_GLC10 suffers some misclassificaiton between impervious surfaces

490 and grassland. Fig. 7R2 shows comparisons over the Payang Lake wetlands. ESA WorldCover captures most marsh

491 wetlands but misses these lake/flooded flats, while ESRI_LC, FROM_GLC10, and GLC_FCS30 have serious

492 omission errors for these wetlands. ESRI_LC misclassifies some marsh wetlands as grassland. Figure 7R3 illustrates

493 comparisons for mountainous areas. ESRI_LC overestimates impervious surfaces, and GLC_FCS30 misses some

494 small impervious surface objects (roads) due to spatial resolution constraints.

495
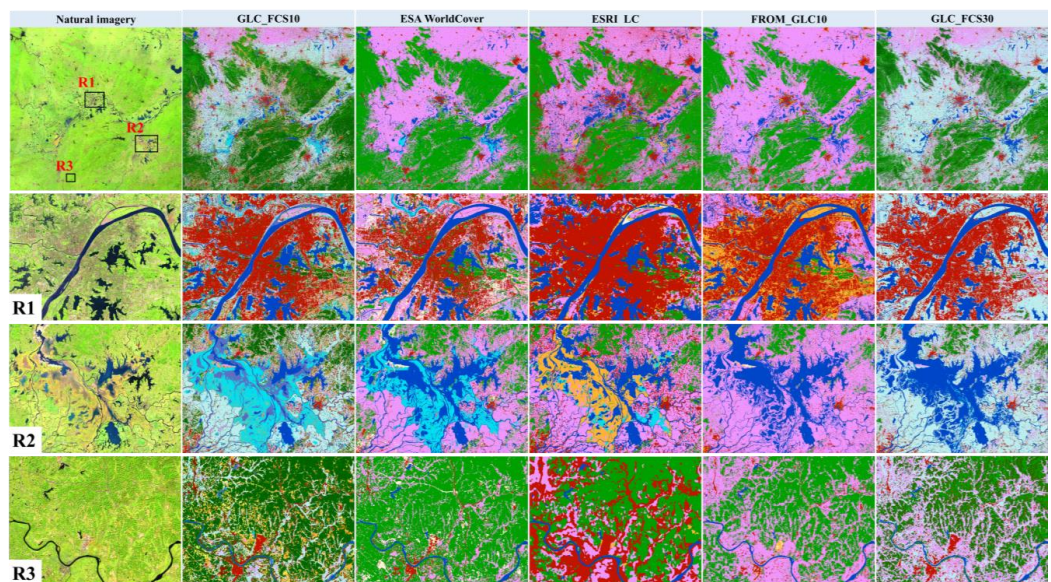
Figure 7. Comparisons among GLC_FCS10 and ESA WorldCover, ESRI_LC, GLC_FCS30, and FROM_GLC10 for the middle reaches of the Yangtze River, China. Images are derived from Sentinel-2 imagery using false-color compositing. The colormap of all land-cover products are same as in Fig. 6.

Because land-cover mapping usually finds tropical areas challenging, Fig. 8 shows comparisons for Kalimantan Island, Indonesia. The region has experienced extensive deforestation and oil palm cultivation over the past few decades (Descals et al., 2024). GLC_FCS10, GLC_FCS30, and FROM_GLC10 can capture the spatial patterns of oil palms because they identify oil palms as cropland, while ESA WorldCover and ESRI_LC tend to treat oil palms as forest. Specifically, in Fig. 8R1, we can see more regular oil palm plantations due to human activities, while FROM_GLC10 and GLC_FCS30 might overestimate the cropland. ESRI_LC and FROM_GLC have serious omission errors on mangroves and swamps for the local region shown in Fig. 8R2, which contains swamp, mangrove, and oil palms, , while ESA WorldCover still cannot identify these swamp wetlands and oil palms, and GLC_FCS30 is consistent with GLC_FCS10 in capturing the wetlands and oil palms.

508
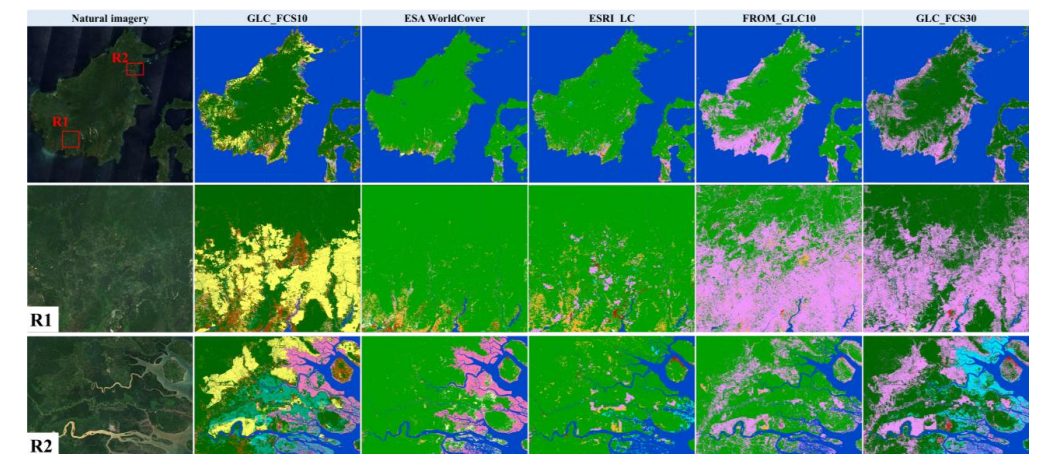
Figure 8. Comparisons between GLC_FCS10 and ESA WorldCover, ESRI_LC, GLC_FCS30, and FROM_GLC10

510 for Kalimantan Island, Indonesia. Images are derived from Sentinel-2 imagery in 2023, and the colormap is the same
511 as in Fig. 6.

4.4 The feasibility and benefits of the proposed method for large-area land-cover mapping

4.4.1 The feasibility and advantages of globally derived training samples

514 A principal difficulty of land-cover mapping is obtaining high-quality training samples (Li et al., 2023; Zhang
515 et al., 2021), in this work, we integrate prior multisource global land-cover products to generate globally distributed
516 training samples. To ensure the confidence of these derived training samples and minimize the classification errors
517 of each prior product, we took the following actions: Spatiotemporal consistency checking was used to find
518 homogeneous and stable areas. The intersection of multiple land-cover products minimized the influence of
519 classification errors in each product. A morphological erosion filter was applied to reduce the impact of edge-mixing
520 effects. The accuracy assessment partly demonstrates the reliability of these derived training samples, i.e.,
521 GLC_FCS10 achieves satisfactory accuracy metrics and outperforms several other land-cover products. Similarly,
522 Zhang et al. (2021) also used the prior global land-cover products to generate the GLC_FCS30 product with
523 satisfactory performance. Due to the large volume of these globally distributed training samples, we selected
524 approximately 10,000 derived samples from the training sample pool in Section 3.2.4. Upon meticulous inspection,
525 we determined that these chosen samples attained an Overall Accuracy (O.A.) of 92.18%, with certain uncertainties
526 existing for shrubland and grassland. This result was in accordance with the earlier analysis presented in Table 3.

527 Moreover, it is still uncertain whether this small amount of erroneous training samples could impact the
528 performance of land-cover mapping, Fig. 9 illustrates the quantitative relationship between the erroneous training
529 samples and the O.A. and kappa coefficients for the basic classification system. Initially, O.A. and the kappa
530 coefficient remain stable as the number of erroneous training samples increases. However, a significant decline occurs
531 when the proportion of erroneous samples exceeds 30%. This indicates that the trained random forest model is robust
532 to the erroneous training samples as long as their proportion remains below 30%. In this work, if the fraction of
533 erroneous samples was kept below 30%, the difference in O.A. is approximately 2% and the decrease in the kappa
534 coefficient is approximately 3%. Gong et al. (2024) also demonstrated that a small number of incorrect samples
535 (approximately 20%) didn't affect the land-cover classification accuracy.
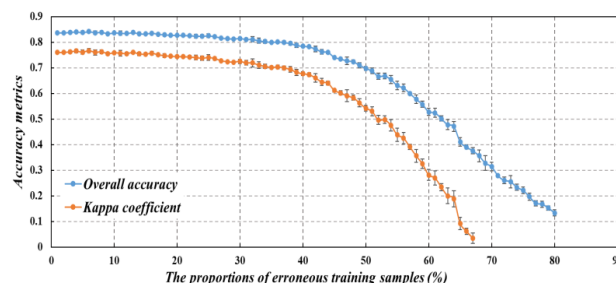
537 **Figure 9**. A sensitive analysis of kappa coefficient and O.A. with respect to the proportion of erroneous training
538 samples.

4.4.2 The advantages of hierarchical land-cover mapping strategy

540 One of the novelties of this study is the adoption of the hierarchical land-cover mapping strategy. The accuracy
541 assessment in Table 3 indicates that impervious surfaces have a high U.A. value of 92.70% and P.A. value of 93.76%.
542 The wetlands U.A. and P.A. values are 70.91% and 53.69%, which were superior to those of the other land-cover
543 products in Table 6 and the cross-comparisons in Figs. 6–8. To intuitively understand the advantage of the hierarchical
544 land-cover mapping strategy, a comparative experiment (***ComExp***) has been designed using the training samples

545   from area-fraction allocation (Fig. 10), i.e., the impervious surfaces and wetlands are not classified separately in the
546   middle reaches of the Yangtze River (the comparative site in Fig. 6). Overall, the ***ComExp*** is consistent with the
547   GLC_FCS10 spatial patterns and shows some variations in the details. Specifically, in Fig. 10R1, the ***ComExp***
548   misclassifies some marsh wetlands as herbaceous rainfed cropland. Some lake flats (red rectangles in Fig. 10R1)
549   cannot be comprehensively captured when compared with the GLC_FCS10. Figure 10R2 gives the comparisons on
550   the impervious surface areas, we can find that the ***ComExp*** has lower impervious surface areas because it
551   misclassifies some bright impervious surfaces as bare areas and some residential areas as vegetated land. In summary,
552   the hierarchical land-cover mapping strategy can increase the ability to characterize specific land-cover types. Sulla-
553   Menashe et al. (2019) also used hierarchical mapping to generate annual global land-cover types for MCD12Q1 and
554   demonstrated its better performance.

555
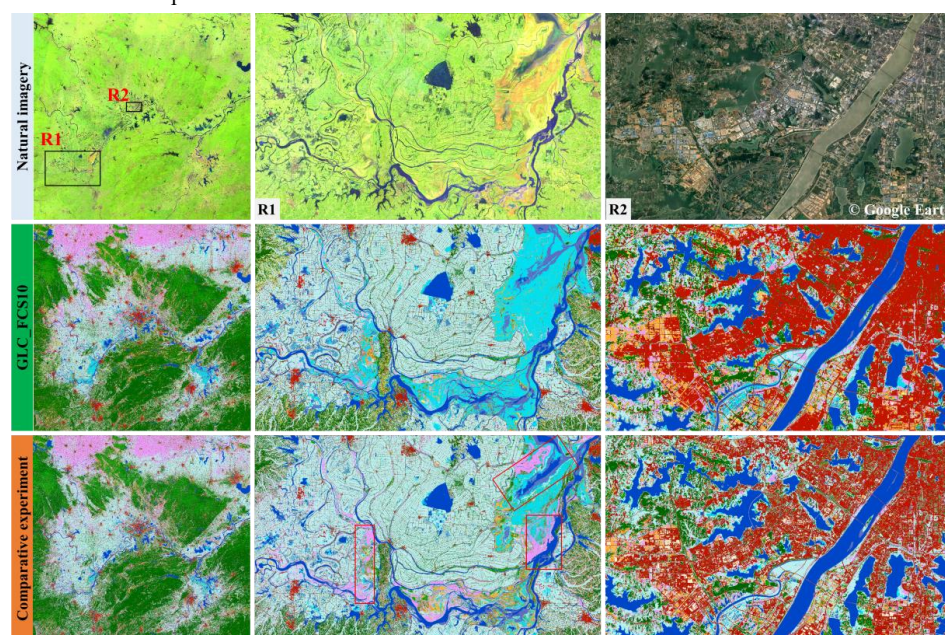
Figure 10. A comparative experiment on whether to adopt the hierarchical land-cover mapping strategy over the
middle reaches of the Yangtze River. Images are composited from Sentinel-2 imagery, and the enlargement came
from © Google Earth. The colormap is the same as in Fig. 6.

4.5 The limitations and prospects

560   By combining a globally distributed training sample pool and the hierarchical land-cover mapping strategy, a
561   novel GLC_FCS10 product containing 30 category-detailed land-cover types has been produced. GLC_FCS10
562   achieves more accurate performance than several previous products in quantitative and qualitative comparisons
563   (Sections 4.2 and 4.3). However, there are still some limitations or uncertainties regarding the proposed method and
564   the developed products, which will be addressed in our ongoing works. First, although we combined hierarchical
565   land-cover mapping and multisource satellite observations to improve the recognition of complicated land-cover
566   types (impervious surfaces and wetlands), however, it can be found that the accuracy metrics of shrubland, grassland
567   and wetland still have substantial room for improvement. Recently, some efforts have shown that incorporating both
568   climatic and land - form factors can enhance the discrimination of grassland areas (Parente et al., 2024) and the
569   combination of Lidar and optical information increases the separability of shrubland and forest (Prošek and Šímová,
570   2019). Thus, one of the further works will combine multisource information to enhance the ability to recognize

571 complex land-cover types.

572 We collected a globally distributed validation dataset and one third-party validation dataset (LCMAP_Val) for
573 the purpose of quantifying the performance of the GLC_FCS10. However, the accuracy metrics of GLC_FCS10 for
574 the fine classification system (containing 30 land-cover types) is still unknown. Actually, some previous studies have
575 emphasized that collecting a large-area validation dataset is quite challenging (Tsendbazar et al., 2021; Xu et al.,
576 2020), especially as this study also needed to focus on 30 fine land-cover types. Fortunately, over the past decades,
577 many previous works have collected high-quality validation points at global or regional scales (d'Andrimont et al.,
578 2020; Li et al., 2017; Stanimirova et al., 2023; Stehman et al., 2012; Zhao et al., 2023). Making full use of these prior
579 knowledge bases to refine the globally distributed validation points into 30 fine land-cover types will be another
580 focus for ongoing work.

581 Last, in order to maximize the utilization of training samples distributed worldwide and strengthen the
582 classification modeling capacity to capture regional characteristics, the local adaptive modeling strategy (Section 3.4)
583 was applied in each 5×5 geographical tile, i.e., the global land-cover maps were produced as 984 independent local
584 adaptive models. There may be a slight spatial discontinuity in some local land-cover maps between neighboring
585 areas even though we introduced spatial neighborhood information into the regional modeling. Thus, further work
586 will take some measures to join global and regional sample modeling to enhance the spatial continuity of global land-
587 cover maps.

588 **5. Data availability**

589 In this study, the novel GLC_FCS10 land-cover dataset with the fine classification system in 2023 has been
590 uploaded to the Zenodo platform and can be visually visited at https://zhangxiao-
591 glcproj.users.earthengine.app/view/glcfcs102023maps and freely access at
592 https://doi.org/10.5281/zenodo.14729665 (Liu and Zhang, 2025). To facilitate the use of this dataset, the global
593 GLC_FCS10 dataset has been stored by a total of 983 independent 5 ×5 geographical tiles, and the tile names as
594 "GLC_FCS10_2023_E/W***N/S##," in which the "***" and "##" illustrate coordinates of longitude and latitude at
595 the upper - left corner of the tile data.

596 As the collection of global validation dataset is labor intensive and time-consuming, our globally distributed
597 validation dataset in 2023 will be available upon reasonable request.

598 **6. Conclusion**

599 The continuous improvement of satellite techniques and computational capability provides ample opportunity
600 for high-resolution global land-cover mapping. In this work, we proposed a framework that leverages prior
601 multisource land-cover products, hierarchical land-cover mapping, and local adaptive classification to generate a
602 novel GLC_FCS10 global land-cover product containing 30 fine land-cover types in 2023 from time-series Sentinel-
603 1 and Sentinel-2 imagery on the GEE platform. The GLC_FCS10 was validated to achieve an O.A. of 83.16% and
604 a kappa coefficient of 0.789 using 56121 globally distributed validation points and achieved an O.A. of 85.09%
605 in the United States using a third-party validation dataset. Furthermore, cross-comparisons with several public
606 global high-resolution land-cover products also demonstrated that GLC_FCS10 had advantages on the diversity
607 of land-cover types and capturing spatial details. Therefore, the GLC_FCS10 is a novel global 10-m land-cover
608 product with high accuracy and a fine classification system. It can provide vital support for high-resolution land-
609 cover applications.

610 **Acknowledgment**

611 We extend our sincere gratitude to all the data providers and organizations whose datasets have been utilized in our

612 research paper, the cloud computing power provided by GEE, and the free storage services offered by the Zenodo

613 platform.

Author contributions

615 The concept and investigation of the project were carried out by LL and XZ. XZ and XC devised the research

616 methodology. TZ, WZ, and MB were responsible for conducting the validation. XZ took the lead in drafting the initial

617 version of the paper. LL and LG engaged in the review and editing process of the paper.

Financial support

619 This research was supported by the National Key Research and Development Program of China (2024YFF0808301)

620 and the National Natural Science Foundation of China (42201499).

Competing interests

622 The corresponding author has declared that none of the authors have any competing interests.

References

624 Azzari, G. and Lobell, D. B.: Landsat-based classification in the cloud: An opportunity for a paradigm shift in land cover

625 monitoring, Remote Sensing of Environment, 202, 64-74, https://doi.org/10.1016/j.rse.2017.05.025, 2017.

626 Ban, Y., Gong, P., and Giri, C.: Global land cover mapping using Earth observation satellite data: Recent progresses and

627 challenges, ISPRS Journal of Photogrammetry and Remote Sensing, 103, 1-6,

628 https://doi.org/10.1016/j.isprsjprs.2015.01.001, 2015.

629 Belgiu, M. and Drăguţ, L.: Random forest in remote sensing: A review of applications and future directions, ISPRS Journal

630 of Photogrammetry and Remote Sensing, 114, 24-31, https://doi.org/10.1016/j.isprsjprs.2016.01.011, 2016.

631 Berger, M., Moreno, J., Johannessen, J. A., Levelt, P. F., and Hanssen, R. F.: ESA's sentinel missions in support of Earth

632 system science, Remote Sensing of Environment, 120, 84-90, https://doi.org/10.1016/j.rse.2011.07.023, 2012.

633 Blickensdörfer, L., Schwieder, M., Pflugmacher, D., Nendel, C., Erasmi, S., and Hostert, P.: Mapping of crop types and

634 crop sequences with combined time series of Sentinel-1, Sentinel-2 and Landsat 8 data for Germany, Remote Sensing of

635 Environment, 269, 112831, https://doi.org/10.1016/j.rse.2021.112831, 2022.

636 Breiman, L.: Random Forests, Machine Learning, 45, 5-32, https://doi.org/10.1023/A:1010933404324, 2001.

637 Brown, C. F., Brumby, S. P., Guzder-Williams, B., Birch, T., Hyde, S. B., Mazzariello, J., Czerwinski, W., Pasquarella, V.

638 J., Haertel, R., Ilyushchenko, S., Schwehr, K., Weisse, M., Stolle, F., Hanson, C., Guinan, O., Moore, R., and Tait, A. M.:

639 Dynamic World, Near real-time global 10 m land use land cover mapping, Scientific Data, 9,

640 https://doi.org/10.1038/s41597-022-01307-4, 2022.

641 Buchhorn, M., Lesiv, M., Tsendbazar, N.-E., Herold, M., Bertels, L., and Smets, B.: Copernicus Global Land Cover

642 Layers—Collection 2, Remote Sensing, 12, 1044, https://doi.org/10.3390/rs12061044, 2020.

643 Bullock, E. L., Healey, S. P., Yang, Z., Houborg, R., Gorelick, N., Tang, X., and Andrianirina, C.: Timeliness in forest

644 change monitoring: A new assessment framework demonstrated using Sentinel-1 and a continuous change detection

645 algorithm, Remote Sensing of Environment, 276, 113043, https://doi.org/10.1016/j.rse.2022.113043, 2022.

646 Bunting, P., Rosenqvist, A., Hilarides, L., Lucas, R. M., Thomas, N., Tadono, T., Worthington, T. A., Spalding, M., Murray,

647 N. J., and Rebelo, L.-M.: Global Mangrove Extent Change 1996–2020: Global Mangrove Watch Version 3.0, Remote

648 Sensing, 14, 3657, https://doi.org/10.3390/rs14153657, 2022.

649 Chen, J., Chen, J., Liao, A., Cao, X., Chen, L., Chen, X., He, C., Han, G., Peng, S., Lu, M., Zhang, W., Tong, X., and Mills,

650 J.: Global land cover mapping at 30m resolution: A POK-based operational approach, ISPRS Journal of Photogrammetry

651 and Remote Sensing, 103, 7-27, https://doi.org/10.1016/j.isprsjprs.2014.09.002, 2015.

652   d'Andrimont, R., Verhegghen, A., Meroni, M., Lemoine, G., Strobl, P., Eiselt, B., Yordanov, M., Martinez-Sanchez, L., and
653   van der Velde, M.: LUCAS Copernicus 2018: Earth Observation relevant in-situ data on land cover throughout the
654   European Union, https://doi.org/10.5194/essd-2020-178, 2020.
655   Dabrowska-Zielinska, K., Musial, J., Malinska, A., Budzynska, M., Gurdak, R., Kiryla, W., Bartold, M., and Grzybowski,
656   P.: Soil Moisture in the Biebrza Wetlands Retrieved from Sentinel-1 Imagery, Remote Sensing, 10, 1979,
657   https://doi.org/10.3390/rs10121979, 2018.
658   Defourny, P., Kirches, G., Brockmann, C., Boettcher, M., Peters, M., Bontemps, S., Lamarche, C., Schlerf, M., and M., S.:
659   Land Cover CCI: Product User Guide Version 2, 2018. 2018.
660   Descals, A., Gaveau, D. L. A., Wich, S., Szantoi, Z., and Meijaard, E.: Global mapping of oil palm planting year from 1990
661   to 2021, Earth Syst. Sci. Data, 16, 5111-5129, https://doi.org/10.5194/essd-16-5111-2024, 2024.
662   Dong, J., Xiao, X., Kou, W., Qin, Y., Zhang, G., Li, L., Jin, C., Zhou, Y., Wang, J., Biradar, C., Liu, J., and Moore, B.:
663   Tracking the dynamics of paddy rice planting area in 1986–2010 through time series Landsat images and phenology-based
664   algorithms, Remote Sensing of Environment, 160, 99-113, https://doi.org/10.1016/j.rse.2015.01.004, 2015.
665   Du, P., Samat, A., Waske, B., Liu, S., and Li, Z.: Random Forest and Rotation Forest for fully polarized SAR image
666   classification using polarimetric and spatial features, Isprs Journal of Photogrammetry & Remote Sensing, 105, 38-53,
667   https://doi.org/10.1016/j.isprsjprs.2015.03.002, 2015.
668   Du, Z., Yu, L., Yang, J., Xu, Y., Chen, B., Peng, S., Zhang, T., Fu, H., Harris, N., and Gong, P.: A global map of planting
669   years of plantations, Scientific Data, 9, https://doi.org/10.1038/s41597-022-01260-2, 2022.
670   Foley, J. A., Defries, R., Asner, G. P., Barford, C., Bonan, G., Carpenter, S. R., Chapin, F. S., Coe, M. T., Daily, G. C.,
671   Gibbs, H. K., Helkowski, J. H., Holloway, T., Howard, E. A., Kucharik, C. J., Monfreda, C., Patz, J. A., Prentice, I. C.,
672   Ramankutty, N., and Snyder, P. K.: Global consequences of land use, Science, 309, 570-574,
673   https://doi.org/10.1126/science.1111772, 2005.
674   Foody, G. M. and Arora, M. K.: An evaluation of some factors affecting the accuracy of classification by an artificial neural
675   network, International Journal of Remote Sensing, 18, 799-810, https://doi.org/10.1080/014311697218764, 2010.
676   Friedl, M. A., Sulla-Menashe, D., Tan, B., Schneider, A., Ramankutty, N., Sibley, A., and Huang, X.: MODIS Collection 5
677   global land cover: Algorithm refinements and characterization of new datasets, Remote Sensing of Environment, 114, 168-
678   182, https://doi.org/10.1016/j.rse.2009.08.016, 2010.
679   Ghorbanian, A., Kakooei, M., Amani, M., Mahdavi, S., Mohammadzadeh, A., and Hasanlou, M.: Improved land cover map
680   of Iran using Sentinel imagery within Google Earth Engine and a novel automatic workflow for land cover classification
681   using migrated training samples, ISPRS Journal of Photogrammetry and Remote Sensing, 167, 276-288,
682   https://doi.org/10.1016/j.isprsjprs.2020.07.013, 2020.
683   Giri, C., Pengra, B., Long, J., and Loveland, T. R.: Next generation of global land cover characterization, mapping, and
684   monitoring, International Journal of Applied Earth Observation and Geoinformation, 25, 30-37,
685   https://doi.org/10.1016/j.jag.2013.03.005, 2013.
686   Gislason, P. O., Benediktsson, J. A., and Sveinsson, J. R.: Random Forests for land cover classification, Pattern Recognition
687   Letters, 27, 294-300, https://doi.org/10.1016/j.patrec.2005.08.011, 2006.
688   Gong, P., Liu, H., Zhang, M., Li, C., Wang, J., Huang, H., Clinton, N., Ji, L., Li, W., Bai, Y., Chen, B., Xu, B., Zhu, Z.,
689   Yuan, C., Ping Suen, H., Guo, J., Xu, N., Li, W., Zhao, Y., Yang, J., Yu, C., Wang, X., Fu, H., Yu, L., Dronova, I., Hui, F.,
690   Cheng, X., Shi, X., Xiao, F., Liu, Q., and Song, L.: Stable classification with limited sample: transferring a 30-m resolution
691   sample set collected in 2015 to mapping 10-m resolution global land cover in 2017, Science Bulletin, 64, 370-373,
692   https://doi.org/10.1016/j.scib.2019.03.002, 2019.
693   Gong, P., Wang, J., and Huang, H.: Stable classification with limited samples in global land cover mapping: Theory and
694   experiments, Science Bulletin, https://doi.org/10.1016/j.scib.2024.03.040, 2024.
695   Gong, P., Wang, J., Yu, L., Zhao, Y., Zhao, Y., Liang, L., Niu, Z., Huang, X., Fu, H., Liu, S., Li, C., Li, X., Fu, W., Liu, C.,

696 Xu, Y., Wang, X., Cheng, Q., Hu, L., Yao, W., Zhang, H., Zhu, P., Zhao, Z., Zhang, H., Zheng, Y., Ji, L., Zhang, Y., Chen,
697 H., Yan, A., Guo, J., Yu, L., Wang, L., Liu, X., Shi, T., Zhu, M., Chen, Y., Yang, G., Tang, P., Xu, B., Giri, C., Clinton, N.,
698 Zhu, Z., Chen, J., and Chen, J.: Finer resolution observation and monitoring of global land cover: first mapping results with
699 Landsat TM and ETM+ data, International Journal of Remote Sensing, 34, 2607-2654,
700 https://doi.org/10.1080/01431161.2012.748992, 2013.
701 Hansen, M. C., Egorov, A., Potapov, P. V., Stehman, S. V., Tyukavina, A., Turubanova, S. A., Roy, D. P., Goetz, S. J.,
702 Loveland, T. R., Ju, J., Kommareddy, A., Kovalskyy, V., Forsyth, C., and Bents, T.: Monitoring conterminous United States
703 (CONUS) land cover change with Web-Enabled Landsat Data (WELD), Remote Sensing of Environment, 140, 466-484,
704 https://doi.org/10.1016/j.rse.2013.08.014, 2014.
705 Homer, C., Dewitz, J., Jin, S., Xian, G., Costello, C., Danielson, P., Gass, L., Funk, M., Wickham, J., Stehman, S., Auch,
706 R., and Riitters, K.: Conterminous United States land cover change patterns 2001–2016 from the 2016 National Land Cover
707 Database, ISPRS Journal of Photogrammetry and Remote Sensing, 162, 184-199,
708 https://doi.org/10.1016/j.isprsjprs.2020.02.019, 2020.
709 Huang, X., Song, Y., Yang, J., Wang, W., Ren, H., Dong, M., Feng, Y., Yin, H., and Li, J.: Toward accurate mapping of 30-
710 m time-series global impervious surface area (GISA), International Journal of Applied Earth Observation and
711 Geoinformation, 109, 102787, https://doi.org/10.1016/j.jag.2022.102787, 2022.
712 Jin, H., Stehman, S. V., and Mountrakis, G.: Assessing the impact of training sample selection on accuracy of an urban
713 classification: a case study in Denver, Colorado, International Journal of Remote Sensing, 35, 2067-2081,
714 https://doi.org/10.1080/01431161.2014.885152, 2014.
715 Karra, K., Kontgis, C., Statman-Weil, Z., Mazzariello, J. C., Mathis, M., and Brumby, S. P.: Global land use / land cover
716 with Sentinel 2 and deep learning, 4704-4707, https://doi.org/10.1109/igarss47720.2021.9553499, 2021.
717 Li, B., Xu, X., Liu, X., Shi, Q., Zhuang, H., Cai, Y., and He, D.: An improved global land cover mapping in 2015 with
718 30 m resolution (GLC-2015) based on a multisource product-fusion approach, Earth Syst. Sci. Data, 15, 2347-
719 2373, https://doi.org/10.5194/essd-15-2347-2023, 2023.
720 Li, C., Peng, G., Wang, J., Zhu, Z., Biging, G. S., Yuan, C., Hu, T., Zhang, H., Wang, Q., and Li, X.: The first all-season
721 sample set for mapping global land cover with Landsat-8 data, Science Bulletin, 62, 508-515,
722 https://doi.org/10.1016/j.scib.2017.03.011, 2017.
723 Li, X., Gong, P., Zhou, Y., Wang, J., Bai, Y., Chen, B., Hu, T., Xiao, Y., Xu, B., Yang, J., Liu, X., Cai, W., Huang, H., Wu,
724 T., Wang, X., Lin, P., Li, X., Chen, J., He, C., Li, X., Yu, L., Clinton, N., and Zhu, Z.: Mapping global urban boundaries
725 from the global artificial impervious area (GAIA) data, Environmental Research Letters, 15, 094044,
726 https://doi.org/10.1088/1748-9326/ab9be3, 2020.
727 Liu, C., Frazier, P., and Kumar, L.: Comparative assessment of the measures of thematic classification accuracy, Remote
728 Sensing of Environment, 107, 606-616, https://doi.org/10.1016/j.rse.2006.10.010, 2007.
729 Liu, L. and Zhang, X.: GLC_FCS10: global 10 m land-cover dataset with fine classification sys tem from Sentinel-1 and
730 2 time-series data, Zenodo [data set]. Zenodo, https://doi.org/10.5281/zenodo.14729665, 2025.
731 Liu, L., Zhang, X., Gao, Y., Chen, X., Shuai, X., and Mi, J.: Finer-Resolution Mapping of Global Land Cover: Recent
732 Developments, Consistency Analysis, and Prospects, Journal of Remote Sensing, 2021, 1-38,
733 https://doi.org/10.34133/2021/5289697, 2021.
734 Mellor, A., Boukir, S., Haywood, A., and Jones, S.: Exploring issues of training data imbalance and mislabelling on random
735 forest performance for large area land cover classification using the ensemble margin, ISPRS Journal of Photogrammetry
736 and Remote Sensing, 105, 155-168, https://doi.org/10.1016/j.isprsjprs.2015.03.014, 2015.
737 Nelson, M. D., Garner, J. D., Tavernia, B. G., Stehman, S. V., Riemann, R. I., Lister, A. J., and Perry, C. H.: Assessing map
738 accuracy from a suite of site-specific, non-site specific, and spatial distribution approaches, Remote Sensing of
739 Environment, 260, 112442, https://doi.org/10.1016/j.rse.2021.112442, 2021.

740 Parente, L., Sloat, L., Mesquita, V., Consoli, D., Stanimirova, R., Hengl, T., Bonannella, C., Teles, N., Wheeler, I., Hunter,
741 M., Ehrmann, S., Ferreira, L., Mattos, A. P., Oliveira, B., Meyer, C., Şahin, M., Witjes, M., Fritz, S., Malek, Z., and Stolle,
742 F.: Annual 30-m maps of global grassland class and extent (2000–2022) based on spatiotemporal Machine Learning,
743 Scientific Data, 11, https://doi.org/10.1038/s41597-024-04139-6, 2024.

744 Pelletier, C., Valero, S., Inglada, J., Champion, N., Marais Sicre, C., and Dedieu, G.: Effect of Training Class Label Noise
745 on Classification Performances for Land Cover Mapping with Satellite Image Time Series, Remote Sensing, 9, 173,
746 https://doi.org/10.3390/rs9020173, 2017.

747 Prošek, J. and Šímová, P.: UAV for mapping shrubland vegetation: Does fusion of spectral and vertical information derived
748 from a single sensor increase the classification accuracy?, International Journal of Applied Earth Observation and
749 Geoinformation, 75, 151-162, https://doi.org/10.1016/j.jag.2018.10.009, 2019.

750 Radeloff, V. C., Roy, D. P., Wulder, M. A., Anderson, M., Cook, B., Crawford, C. J., Friedl, M., Gao, F., Gorelick, N.,
751 Hansen, M., Healey, S., Hostert, P., Hulley, G., Huntington, J. L., Johnson, D. M., Neigh, C., Lyapustin, A., Lymburner, L.,
752 Pahlevan, N., Pekel, J.-F., Scambos, T. A., Schaaf, C., Strobl, P., Woodcock, C. E., Zhang, H. K., and Zhu, Z.: Need and
753 vision for global medium-resolution Landsat and Sentinel-2 data products, Remote Sensing of Environment, 300, 113918,
754 https://doi.org/10.1016/j.rse.2023.113918, 2024.

755 Radoux, J., Lamarche, C., Van Bogaert, E., Bontemps, S., Brockmann, C., and Defourny, P.: Automated Training Sample
756 Extraction for Global Land Cover Mapping, Remote Sensing, 6, 3965-3987, https://doi.org/10.3390/rs6053965, 2014.

757 Rodriguez-Galiano, V. F., Chica-Olmo, M., Abarca-Hernandez, F., Atkinson, P. M., and Jeganathan, C.: Random Forest
758 classification of Mediterranean land cover using multi-seasonal imagery and multi-seasonal texture, Remote Sensing of
759 Environment, 121, 93-107, https://doi.org/10.1016/j.rse.2011.12.003, 2012.

760 Stanimirova, R., Tarrio, K., Turlej, K., McAvoy, K., Stonebrook, S., Hu, K. T., Arevalo, P., Bullock, E. L., Zhang, Y.,
761 Woodcock, C. E., Olofsson, P., Zhu, Z., Barber, C. P., Souza, C. M., Jr., Chen, S., Wang, J. A., Mensah, F., Calderon-Loor,
762 M., Hadjikakou, M., Bryan, B. A., Graesser, J., Beyene, D. L., Mutasha, B., Siame, S., Siampale, A., and Friedl, M. A.: A
763 global land cover training dataset from 1984 to 2020, Sci Data, 10, 879, https://doi.org/10.1038/s41597-023-02798-5, 2023.

764 Stehman, S. V., Olofsson, P., Woodcock, C. E., Herold, M., and Friedl, M. A.: A global land-cover validation data set, II:
765 augmenting a stratified sampling design to estimate accuracy by region and land-cover class, International Journal of
766 Remote Sensing, 33, 6975-6993, https://doi.org/10.1080/01431161.2012.695092, 2012.

767 Stehman, S. V., Pengra, B. W., Horton, J. A., and Wellington, D. F.: Validation of the U.S. Geological Survey's Land Change
768 Monitoring, Assessment and Projection (LCMAP) Collection 1.0 annual land cover products 1985–2017, Remote Sensing
769 of Environment, 265, 112646, https://doi.org/10.1016/j.rse.2021.112646, 2021.

770 Sulla-Menashe, D., Gray, J. M., Abercrombie, S. P., and Friedl, M. A.: Hierarchical mapping of annual global land cover
771 2001 to present: The MODIS Collection 6 Land Cover product, Remote Sensing of Environment, 222, 183-194,
772 https://doi.org/10.1016/j.rse.2018.12.013, 2019.

773 Tachikawa, T., Kaku, M., Iwasaki, A., Gesch, D. B., Oimoen, M. J., Zhang, Z., Danielson, J., Krieger, T., Curtis, B., and
774 Haase, J.: ASTER Global Digital Elevation Model Version 2 – Summary of validation results, Kim Fakultas Sastra Dan
775 Budaya, https://doi.org/10.1093/oxfordjournals.pubmed.a024792, 2011.

776 Tang, X., Bratley, K. H., Cho, K., Bullock, E. L., Olofsson, P., and Woodcock, C. E.: Near real-time monitoring of tropical
777 forest disturbance by fusion of Landsat, Sentinel-2, and Sentinel-1 data, Remote Sensing of Environment, 294, 113626,
778 https://doi.org/10.1016/j.rse.2023.113626, 2023.

779 Torres, R., Snoeij, P., Geudtner, D., Bibby, D., Davidson, M., Attema, E., Potin, P., Rommen, B., Floury, N., Brown, M.,
780 Traver, I. N., Deghaye, P., Duesmann, B., Rosich, B., Miranda, N., Bruno, C., L'Abbate, M., Croci, R., Pietropaolo, A.,
781 Huchler, M., and Rostan, F.: GMES Sentinel-1 mission, Remote Sensing of Environment, 120, 9-24,
782 https://doi.org/10.1016/j.rse.2011.05.028, 2012.

783 Tsendbazar, N., Herold, M., Li, L., Tarko, A., de Bruin, S., Masiliunas, D., Lesiv, M., Fritz, S., Buchhorn, M., Smets, B.,

784   Van De Kerchove, R., and Duerauer, M.: Towards operational validation of annual global land cover maps, Remote Sensing
785   of Environment, 266, 112686, https://doi.org/10.1016/j.rse.2021.112686, 2021.

786   Wang, Y., Sun, Y., Cao, X., Wang, Y., Zhang, W., and Cheng, X.: A review of regional and Global scale Land Use/Land
787   Cover (LULC) mapping products generated from satellite remote sensing, ISPRS Journal of Photogrammetry and Remote
788   Sensing, 206, 311-334, https://doi.org/10.1016/j.isprsjprs.2023.11.014, 2023.

789   Wickham, J., Stehman, S. V., Sorenson, D. G., Gass, L., and Dewitz, J. A.: Thematic accuracy assessment of the NLCD
790   2016 land cover for the conterminous United States, Remote Sensing of Environment, 257, 112357,
791   https://doi.org/10.1016/j.rse.2021.112357, 2021.

792   Wilen, B. O. and Bates, M.: The US fish and wildlife service's national wetlands inventory project. In: Classification and
793   inventory of the world's wetlands, Springer, https://doi.org/10.1007/978-94-011-0427-2_13, 1995.

794   Worthington, T. A., Spalding, M., Landis, E., Maxwell, T. L., Navarro, A., Smart, L. S., and Murray, N. J.: The distribution
795   of global tidal marshes from Earth observation data, Global Ecology and Biogeography, https://doi.org/10.1111/geb.13852,
796   2024.

797   Xian, G. Z., Smith, K., Wellington, D., Horton, J., Zhou, Q., Li, C., Auch, R., Brown, J. F., Zhu, Z., and Reker, R. R.:
798   Implementation of the CCDC algorithm to produce the LCMAP Collection 1.0 annual land surface change product, Earth
799   Syst. Sci. Data, 14, 143-162, https://doi.org/10.5194/essd-14-143-2022, 2022.

800   Xie, S., Liu, L., and Yang, J.: Time-Series Model-Adjusted Percentile Features: Improved Percentile Features for Land-
801   Cover Classification Based on Landsat Data, Remote Sensing, 12, 3091, https://doi.org/10.3390/rs12183091, 2020.

802   Xu, P., Herold, M., Tsendbazar, N.-E., and Clevers, J. G. P. W.: Towards a comprehensive and consistent global aquatic
803   land cover characterization framework addressing multiple user needs, Remote Sensing of Environment, 250, 112034,
804   https://doi.org/10.1016/j.rse.2020.112034, 2020.

805   Yang, J. and Huang, X.: The 30 m annual land cover dataset and its dynamics in China from 1990 to 2019, Earth Syst. Sci.
806   Data, 13, 3907-3925, https://doi.org/10.5194/essd-13-3907-2021, 2021.

807   Yu, L., Wang, J., Li, X., Li, C., Zhao, Y., and Gong, P.: A multi-resolution global land cover dataset through multisource
808   data aggregation, Science China Earth Sciences, 57, 2317-2329, https://doi.org/10.1007/s11430-014-4919-z, 2014.

809   Zanaga, D., Van De Kerchove, R., De Keersmaecker, W., Souverijns, N., Brockmann, C., Quast, R., Wevers, J., Grosu, A.,
810   Paccini, A., and Vergnaud, S.: ESA WorldCover 10 m 2020 v100, Zenodo: Geneve, Switzerland,
811   https://doi.org/10.5281/zenodo.5571936, 2021.

812   Zhang, H. K. and Roy, D. P.: Using the 500 m MODIS land cover product to derive a consistent continental scale 30 m
813   Landsat land cover classification, Remote Sensing of Environment, 197, 15-34, https://doi.org/10.1016/j.rse.2017.05.024,
814   2017.

815   Zhang, X., Liu, L., Chen, X., Gao, Y., Xie, S., and Mi, J.: GLC_FCS30: global land-cover product with fine classification
816   system at 30 m using time-series Landsat imagery, Earth Syst. Sci. Data, 13, 2753-2776, https://doi.org/10.5194/essd-13-
817   2753-2021, 2021.

818   Zhang, X., Liu, L., Wang, J., Zhao, T., Liu, W., and Chen, X.: Automated Mapping of Global 30-m Tidal Flats Using Time-
819   Series Landsat Imagery: Algorithm and Products, Journal of Remote Sensing, 3,
820   https://doi.org/10.34133/remotesensing.0091, 2023a.

821   Zhang, X., Liu, L., Wu, C., Chen, X., Gao, Y., Xie, S., and Zhang, B.: Development of a global 30 m impervious surface
822   map using multisource and multitemporal remote sensing datasets with the Google Earth Engine platform, Earth Syst. Sci.
823   Data, 12, 1625-1648, https://doi.org/10.5194/essd-12-1625-2020, 2020.

824   Zhang, X., Liu, L., Zhang, W., Guan, L., Bai, M., Zhao, T., Zhehua, L., and Chen, X.: Tracking gain and loss of impervious
825   surfaces by integrating continuous change detection and multitemporal classifications from 1985 to 2022 in Beijing,
826   International Journal of Applied Earth Observation and Geoinformation, 135, 104268,
827   https://doi.org/10.1016/j.jag.2024.104268, 2024a.

828 Zhang, X., Liu, L., Zhao, T., Chen, X., Lin, S., Wang, J., Mi, J., and Liu, W.: GWL_FCS30: a global 30 m wetland map
829 with a fine classification system using multi-sourced and time-series remote sensing imagery in 2020, Earth Syst. Sci. Data,
830 15, 265-293, https://doi.org/10.5194/essd-15-265-2023, 2023b.
831 Zhang, X., Liu, L., Zhao, T., Gao, Y., Chen, X., and Mi, J.: GISD30: global 30 m impervious-surface dynamic dataset from
832 1985 to 2020 using time-series Landsat imagery on the Google Earth Engine platform, Earth Syst. Sci. Data, 14, 1831-
833 1856, https://doi.org/10.5194/essd-14-1831-2022, 2022.
834 Zhang, X., Liu, L., Zhao, T., Wang, J., Liu, W., and Chen, X.: Global annual wetland dataset at 30 m with a fine
835 classification system from 2000 to 2022, Scientific Data, 11, https://doi.org/10.1038/s41597-024-03143-0, 2024b.
836 Zhang, X., Zhao, T., Xu, H., Liu, W., Wang, J., Chen, X., and Liu, L.: GLC_FCS30D: the first global 30 m land-cover
837 dynamics monitoring product with a fine classification system for the period from 1985 to 2022 generated using dense-
838 time-series Landsat imagery and the continuous change-detection method, Earth Syst. Sci. Data, 16, 1353-1381,
839 https://doi.org/10.5194/essd-16-1353-2024, 2024c.
840 Zhao, T., Zhang, X., Gao, Y., Mi, J., Liu, W., Wang, J., Jiang, M., and Liu, L.: Assessing the Accuracy and Consistency of
841 Six Fine-Resolution Global Land Cover Products Using a Novel Stratified Random Sampling Validation Dataset, Remote
842 Sensing, 15, 2285, https://doi.org/10.3390/rs15092285, 2023.
843 Zhu, Z., Gallant, A. L., Woodcock, C. E., Pengra, B., Olofsson, P., Loveland, T. R., Jin, S., Dahal, D., Yang, L., and Auch,
844 R. F.: Optimizing selection of training and auxiliary data for operational land cover classification for the LCMAP initiative,
845 ISPRS Journal of Photogrammetry and Remote Sensing, 122, 206-221, https://doi.org/10.1016/j.isprsjprs.2016.11.004,
846 2016.
847